UNIVERSITY OF GOTHENBURG

SAHLGRENSKA ACADEMY

Preprocessing for intravoxel incoherent motion analysis in the brain

Signal drift correction

Amina Warsame

Essay/Thesis:	30 hp
Program and/or course:	Medical physics
Level:	Second Cycle
Term/year:	Fall 2022
Supervisors:	Oscar Jalnefjord, Louise Rosenqvist
Examiner:	Magnus Båth

Preprocessing for intravoxel incoherent motion analysis in the brain

Signal drift correction

Amina Warsame

Sahlgrenska Academy
University of Gothenburg
Gothenburg, Sweden 2023

Preprocessing for intravoxel incoherent motion analysis in the brain
Signal drift correction

Supervisors: Oscar Jalnefjord, Department of Medical Radiation Sciences,
Louise Rosenqvist, Department of Medical Radiation Sciences.
Examiner: Magnus Båth, Department of Medical Radiation Sciences.

Master's Thesis 2023
Sahlgrenska Academy
University of Gothenburg

Typeset in LaTeX
Gothenburg, Sweden 2023

Preprocessing for intravoxel incoherent motion analysis in the brain
Signal drift correction

Amina Warsame
Sahlgrenska Academy
University of Gothenburg

Abstract

Diffusion magnetic resonance imaging (dMRI) is a diagnostic imaging technique that is sensitized to the movement of water molecules in tissues. Intravoxel incoherent motion (IVIM) analysis can be used to estimate blood flow in capillaries from weakly diffusion-weighted data. dMRI images can be impacted by confounding factors and are usually preprocessed to improve their quality.

This study reviewed the preprocessing pipeline for dMRI in relation to IVIM analysis in the brain. The results showed that the necessary preprocessing steps for IVIM analysis can be challenging due to a lack of consensus in this field, and may vary depending on the data and circumstances. While various tools for preprocessing dMRI exist, most of these tools are designed for datasets that have stronger diffusion-weighted data and more diffusion-encoding gradient directions than those typically used in IVIM. The results showed that only a limited number of these preprocessing tools can be directly applied to IVIM datasets. Based on observerations in previously acquired data, an in-depth analysis of the effect of signal drift on IVIM data was also investigated, and two correction methods were evaluated: temporal correction and spatio-temporal correction. Results from the signal drift study showed that the temporal and the spatio-temporal correction methods can reduce or amplify the effects of signal drift in IVIM data. This may indicate that additional methods may be needed to fully correct for this issue and obtain reliable results from IVIM imaging. In conclusion, it is crucial to have a thorough understanding of the data and desired results in order to accurately correct data.

Keywords: MRI, Diffusion, Perfusion, Diffusion-weighted imaging.

Sammanfattning

Diffusionsviktad MR (dMRI) är en bildgivande teknik som är känslig för rörelsen av vattenmolekyler i vävnader. Analys av inkoherent rörelse inom en voxel (IVIM) kan användas för att uppskatta blodflödet i kapillärer från svagt diffusionsviktad data. dMRI-data kan påverkas av störningar och genomgår preprocessing vanligtvis för att förbättra deras kvalitet.

Denna studie undersökte preprocessing stegen för dMRI i förhållande till IVIM-analys i hjärna. I arbetet undersöktes även effekten av signaldrift på IVIM-data och två korrektionsmetoder utvärderades: temporal korrektion och spatio-temporal korrektion. Resultaten visade att det kan vara utmanande att fastställa de nödvändiga preprocessingstegen för IVIM-data på grund av bristande konsensus inom området. Därmed kan antalet steg variera beroende på data och omständigheter. Trots det faktum att flera väletablerade verktyg för preprocessering för dMRI existerar, är de flesta verktyg utformade för datamängder med starkare diffusionsviktning och fler diffusionkodningsgradientriktningar än de som vanligtvis används för IVIM. Resultaten visade att endast ett begränsat antal verktyg direkt kan tillämpas på IVIM-data. Baserat på observationer från tidigare studier har en undersökning om effekten av signaldrift i IVIM-data studerats, där två korrektionsmetoder har utvärderats: temporal korrektion och Spatio-temporal korrektion. Resultatet visade att både temporal och spatio-temporala korrektionsmetoderna kan minska eller öka effekten av signaldrift i IVIM-data, vilket kan indikera på att ytterligare metoder kan behövas för att fullständigt korrigera för ostabiliteten i signalen. Sammanfattningsvis är det viktigt att ha en djup förståelse av den erhållna data och det önskade resultatet för att korrigera data på ett korrekt sätt.
.

Acknowledgements

Bismillah, I would like to begin by thanking Allah for providing me with the knowledge and opportunity to undertake this research and for blessing me with the many gems of wisdom that I have gained along the way.

Secondly, I would like to express my sincere gratitude to my supervisors, Oscar Jalnefjord and Louise Rosenqvist, for their guidance, support, and encouragement throughout my thesis on signal drift correction for intravoxel incoherent motion analysis in the brain. Their expertise in coding and research methodology were invaluable in helping me determine the most appropriate approach for this thesis. I also appreciate their patience and belief in me, which allowed me to push through any challenges and complete my thesis successfully.

I would also like to thank all the participants in my study for their time and willingness to contribute to my thesis. Without their valuable input, this work would not have been possible.

Lastly, I am deeply grateful to my family and friends for their unwavering support and encouragement throughout my academic journey. Their love and guidance have been a constant source of strength and motivation for me.

Thank you!

Contents

1
Introduction

Magnetic resonance imaging (MRI) is a highly valuable diagnostic tool in medical imaging, capable of producing detailed images of the human body using a strong magnetic field and radio waves. Unlike many other imaging modalities such as computed tomography (CT), MRI does not expose the patient to ionizing radiation, making it a safe option for repeated or long-term imaging. One specific application of MRI, called diffusion magnetic resonance imaging (dMRI), utilizes the signal from an MR image that is sensitive to the random motions of water in tissues through various strengths of diffusion encoding. This method is widely used clinically for various investigations, such as cerebral ischemia and cancer. There is also growing clinical interest in using dMRI for perfusion imaging due to its potential to exclude contrast media in situations where the use of contrast agents is restricted or undesirable [1].

The MR signal obtained from in vivo dMRI is not a pure representation of diffusion, as it also includes signals from microcirculation in the capillaries, which is most noticeable at weaker diffusion encoding. Le Bihan et al. were first to present a method to separate the effects of diffusion and perfusion on the dMRI signal [2]. Intravoxel incoherent motion (IVIM) is the model that is used to quantify as well as separate diffusion and perfusion effects, observed at weaker diffusion encoding.

IVIM is a non-invasive approach for quantifying perfusion and is currently in the development stages and is not yet in routine clinical use. The method allows for the reconstruction of different parameter maps which characterize, for example, the movement of water molecules in blood and the perfusion fraction which offers a measure of how much blood is within a voxel. Estimating IVIM parameters is a difficult task in general, especially in the brain, where the proportion of signal from blood is only around 5% [3]. Obtaining reliable parameter estimates from the low perfusion signal require minimizing any disturbances in the estimates. This often requires correcting the data for various factors that can improperly impact the signal. Signal drift, which refers to the decrease or increase in signal magnitude in subsequently acquired images within a scan session, is one such factor that has been found to affect the signal. A study by Vos et al. (2017) demonstrated that within a 15-minute scan session of a phantom, a signal drift of 5-6% can be observed [4].

It is common practice to preprocess dMRI data before proceeding to analysis, since these images often are prone to artefacts [5]. Preprocessing in this context can be defined as any type of correction made in the image domain or frequency domain after data acquisition and before performing parameter map computations or analysis. Although relatively

well-established tools for preprocessing diffusion-weighted images exists, they are usually developed with a focus on strongly diffusion-weighted images and more diffusion encoding directions than typically used for IVIM.

The primary aim of the thesis was to review the preprocessing pipeline for dMRI and investigate what is relevant for IVIM brain. As signal drift has been observed in IVIM data of the brain acquired by the research group, a secondary aim was to investigate the effect of signal drift on IVIM data and evaluate selected corrections.

2
Diffusion MRI

2.1 Basics of the MR signal

The MR signal originates from the precision of the hydrogen nuclei. The nucleus of a hydrogen atom contains a proton making it a positively charged nucleus. The hydrogen nucleus has a non-zero spin, giving it an angular momentum $\vec{J}$ and an intrinsic magnetic moment $\vec{\mu}$ in the same direction. Inside the human body these hydrogen nucleons are randomly orientated, with no resulting net magnetization in a given direction. When an external magnetic field is applied, as in the case of an MR examination, the protons tend to align parallel with the primary static magnetic field B_0, resulting in a longitudinal net magnetization. Since the protons have spin, they will precess around this axis with the Larmor frequency,

$$\omega_0 = \gamma B_0 \tag{2.1}$$

where γ is the gyromagnetic constant, specific to the isotope.

To get the MR signal, the longitudinally net magnetization is subjected to an orthogonal radio frequency (RF) pulse, which generates a transverse net magnetization (B_1). This is known as excitation. However, this is only true if the frequency of the RF pulse match the precession of the nuclei i.e., the Larmor frequency. After the RF pulse, the protons relax to their longitudinal net magnetization. The amount of energy released during the relaxation process is then measured using receiver coils. This is the MR signal.

By applying gradient magnetic fields in the x, y and z-axis, the strength of B_0 will vary spatially. This will cause the frequency of precession to change and the spin to accumulate phase. The phase shift is determined by the gradient strength and duration. If the strength of the gradient field is constant, stationary nuclei will accumulate phase $\phi_{stationary}$ linearly over time t.

$$\phi_{stationary}(t) = \gamma G x t \tag{2.2}$$

where x is the position of the stationary spin. On the other hand, if the spin is moving with a velocity v, the accumulated phase ϕ_{moving} is described as,

$$\phi_{moving}(t) = \frac{\gamma G v t^2}{2} \tag{2.3}$$

2.2 Diffusion-weighted MR signal

The contrast in a diffusion-weighted MR image is provided by diffusion, which is the random microscopic motion of small molecules caused by thermal energy. The pulse sequence for dMRI is designed to produce images in which tissues with mobile water molecules, such as those with high diffusion, have lower signal amplitudes than tissues with more stationary molecules, such as those with restricted diffusion [6]. In the resulting image, the diffusion restricted areas appear brighter and the areas with higher diffusion appear darker, e.g. cerebrospinal fluid (CSF) will appear darker.

The shape of the diffusion encoding gradients and their strength determine the contrast in a dMRI image. Typically a dMRI sequence consists of a Stejskal-Tanner pulsed gradient spin echo (PGSE) sequence with diffusion gradients. In a PGSE sequence only the non-stationary spins will be influenced by the diffusion gradients. The stationary spin will not experience a net phase shift thus not contributing to the signal decay. The signal loss from the moving spins can therefore be isolated and quantified. By using varying strengths of diffusion-weighting (b-value), it is possible to determine IVIM parameters.

The PGSE sequence is sensitive to perfusion at low b-values. However, it is difficult to estimate perfusion based on this signal, as the percentage of signal from perfusion is very small. On the contrary there are scan sequences sensitive to motion that uses the flow of blood to quantify the perfusion fraction f [7]. By using bipolar gradients (flow encoding gradient) it is possible to obtain either a flow-compensated (FC) image or a non-flow-compensated (NC) image. Two bipolar gradients are used in flow/non-flow compensating acquisitions. The first gradient causes the spins travelling along the gradient to accumulate phase. The second gradient has reversed polarity which rephases the spins moving at constant velocity. As a result, neither stationary nor spin moving at constant velocity in a straight line will experience a net phase shift [6]. The contrast between the FC and NC image depend on perfusion, thus the perfusion fraction can be estimated.

2.2.1 Intravoxel incoherent motion

Intravoxel Incoherent Motion (IVIM) refers to the disorganized motion of hydrogen nuclei spins within a voxel. If the movement is incoherent within a voxel the spins will not obtain the same phase shift. This will result in the spins having a phase distribution, causing signal attenuation and a lower magnitude of the MR signal. Diffusion and perfusion in tissue are examples of incoherent motion that can be visualized using specific MR sequences.

The IVIM model proposed by Le Bihan et al. is based on the assumption that the signal decay comes from two components: perfusion and diffusion [2]. The signal including both effects can be describes as,

$$\frac{S(b)}{S(0)} = \underbrace{f e^{-b(D_{blood}+D^*)}}_{\text{Perfusion}} + \underbrace{(1-f)e^{-bD_{tissue}}}_{\text{Diffusion}} \tag{2.4}$$

where f is the perfusion fraction (the fraction of the signal decay that comes from perfusion), D_{blood} and D_{tissue} [mm^2/s] is the diffusion coefficient of water in blood and tissue, respectively, D^* [mm^2/s] is the pseudo-diffusion coefficient from the incoherent motion of blood in capillaries. b [s/mm^2] is the strength of the diffusion-weighting and can for the commonly used PGSE, be written as,

$$b = \gamma^2 G^2 \delta^2 (\Delta - \frac{\delta}{3}) \tag{2.5}$$

where γ [rad/sT] is the gyromagnetic ratio, G[mT/m] is the gradient amplitude , δ [ms] is the duration of each gradient pulse, Δ [ms] is the spacing between the pulses, see figure 2.1.

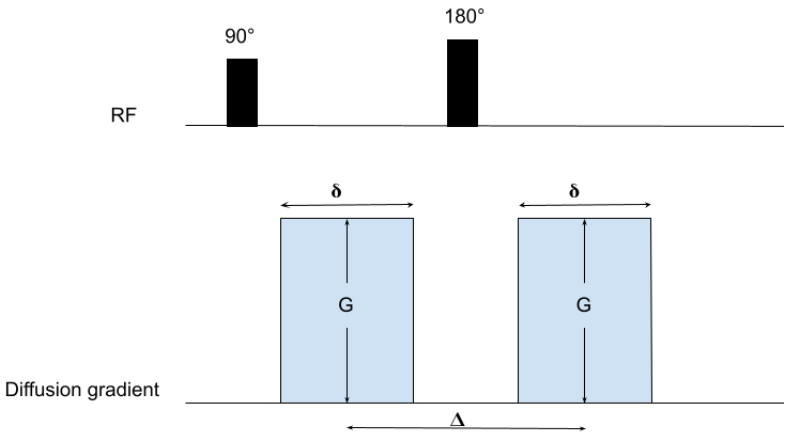

Figure 2.1: An arbitrary spin-echo sequence with diffusion gradients applied, with the magnitude G.

3
Review of preprocessing for dMRI

The preprocessing pipeline for dMRI has not been standardized yet. In a review article about dMRI preprocessing, Tax et al specify 15 different steps in the pipeline for brain images [5]. This chapter aims to discuss and summarize these steps as well as their relevance for IVIM analysis of the brain.

3.1 Brain extraction

Brain extraction is a critical component of any neuroimaging study obtained via magnetic resonance imaging (MRI). The human head not only contains the brain but also other organs and the skull. Therefore, the first preprocessing step is often to extract the brain tissue, removing the skull and non-brain tissues. The extracted brain mask can be utilized both in subsequent preprocessing steps and during analysis. Since the brain extraction is normally performed before any corrections, there could exist some distortions within the image, making the extraction inaccurate.

Consequently, the outcomes of subsequent computations for parameter maps, such as those used to quantify diffusion, are influenced by the brain extraction. Corrections for movement and distortions can especially have a significant influence in the brain extraction. As a result, it may be beneficial to re-extract the brain after preprocessing, before analysis.

Tax et al. (2022) write that the extraction can be reduced to a forward/background segmentation problem for fat-suppressed Echo Planar Imaging (EPI), which is the common choice for dMRI of the brain [5]. This is possible since the signal intensity from fat, muscle tissue and skull are lower than the signal of the brain in a fat-supressed EPI.

The Oxford Centre for Functional MRI of the brain offers a software library (FSL), with a brain extraction tool (BET) [8]. The BET algorithm begins by placing a small sphere at the center of gravity of the head. Based on assumptions about the shape of the brain and by estimating intensity gradients, the sphere is reshaped and updated iteratively until it reaches the inner surface of the skull. When working with dMRI dataset the extraction is performed on a $b0$-image i.e. a non-diffusion-weighted image. As b0-images are also aqcuired during IVIM imaging, the same method for brain extraction can be utilized for IVIM-dataset.

3.2 B-Matrix incompatibility with the imaging data

The B-matrix contains information about diffusion gradient direction and b-value. The diffusion encoding information is usually stored in the DICOM header as a B-matrix or separated into b-value/b-vector pairs. Depending on the manufacturer and scanner, the B-matrix may be stored in a coordinate system other than that used for the image. This may cause mismatch between the coordinate system of the imaging system and the B-matrix. Mismatches can also occur when converting between file types.

The available tools for observing and/or correcting for coordinate system discrepancies are designated for the brain, where it is well understood how the directional dependence of the diffusion should behave. In dMRI, analyzing the diffusion tensor eigenvectors can reveal what happened to the data and how to correct it. This manual inspection can, however, be tedious. As a result, automated methods that check for B-matrix incompatibilities and applies the correction required to match the imaging data's coordinate space, have been suggested. One of these methods utilizes the average fiber trajectory length in the brain, which is used determine how well the gradient orientations match the dMRI images [9]. The assumption is that flipped gradients directions or wrong coordinate system will lead to a reduction in the average fiber trajectory length in the brain. Other similar methods are AFNI GradFlipTest, which also utilizes the fiber track length in the brain [10].

B-matrix incompatibilities might occur in the IVIM-dataset since the mismatch between the B-matrix and imaging data is inherent to all dMRI. Since IVIM often only has three encoding directions while the dMRI data utilizes more, the previously suggested methods, such as GradFlipTEST and the average fiber trajectory, can not in most cases be utilized for IVIM-data. However, the B-matrix incompatibility will generally not be a problem for IVIM-data, given that IVIM typically only analyzes the signal averaged over all encoding directions.

3.3 Signal drift correction

It has been discovered that a systematic increase or decrease in signal intensity can occur during dMRI scanning session, both temporally and spatio-temporally [4, 11]. There are several hypotheses on what causes this, ranging from heating from the gradients in an EPI to frequency drift in the main magnetic field. The problems that might arise from signal drift is overestimation/underestimation of diffusion and systemic bias for different orientations.

There are a few different strategies for adressing the signal drift issue. It has been suggested that non-diffusion-weighted volumes should be distributed throughout the scan. Following that, a model for the signal drift over the scan session is estimated, which is then used to tune the signal [11].

The scope of this thesis includes a study on the presence of signal drift in IVIM-data as

well as ways to correct for it. In chapter 4, both temporal and spatio-temporal corrections are applied and evaluated.

3.4 Gibbs ringing correction

The MRI signal is observed as Fourier coefficients in the spatial frequency domain (k-space). However, because the sampled k-space is finite, a choice is made about which frequencies to sample in order to reconstruct the image. Thus, the reconstructed image is bounded by a finite box-function. During image reconstruction via Fourier transform, the Fourier representation is insufficient for high-contrast interfaces. In the image domain this will result in an image convoluted with a sinc-function. The oscillations of the sinc-function can be observed in the reconstructed image as Gibbs-ringing artifacts, notably at anatomical borders in MRI images. Gibbs-ringing can be minimized with the choice of phase-encoding steps and field-of-view before acquisition. However, since it is an inherent effect of signal representation by a finite number of spatial frequencies, Gibbs-ringing can never be completely eliminated.

There are multiple solutions to deal with Gibbs artifacts post-acquisition. Filters like Gaussian, Hanning or Hamming can be used to smear out the effect. However, as these filters tend to lead to blurry images, other solutions have been proposed, such as sub-voxelshift correction [12]. This method is built on shifting the data point with a fraction of a voxel. The Gibbs ringing artifact can effectively then be minimized by sampling at the zero-crossing of the sinc-function and interpolating the missing data points.

In IVIM imaging, minor changes in the signal are of interest, hence data quality is fundamental. If there is something in the background that might interfere, such as Gibbs artifact, it needs to be addressed.

3.5 Noise distribution bias correction

The noise in a typical MRI image can be approximated as Gaussian distributed, provided that the signal-to-noise ratio (SNR) is not too low. However, in dMRI, the noise distribution could have some other shapes. Particularly, the magnitude of dMRI data is noncentral Chi distributed [13]. This can cause problems in areas with low SNR, resulting in underestimation of diffusivity.

Accurate IVIM parameter estimation requires high SNR. Furthermore, because the SNR of the low b-value dataset is high, the signal does not dip below zero or oscillate around it. As a result, the bias of the noise distribution may not be a significant concern in IVIM imaging.

3.6 Denoising

Thermal noise can visually disturb both strong and weakly diffusion-weighted data and contributes to the uncertainty in the estimates of IVIM parameters. As mentioned in previous sections, minor changes in signal are of interest for IVIM. To detect these small changes, high SNR and low noise is fundamental. It is estimated that a few percent of the signal from IVIM is related to perfusion in the brain, thus any noise in the data can influence the estimated parameter maps [1].

Traditionally, denoising has involved averaging nearby voxels using noise-reducing filters like Gaussian-smoothing filters and adaptive smoothing filter. Recently, machine-learning-based denoising techniques have been developed, such as Patch2Self, which assumes the noise is uncorrelated noise [14]. Both filtering and machine-learning methods may be used for IVIM. Other methods are based on Principle Component Analysis (PCA), which works on the assumption that the dMRI data is oversampled and only a few principal components are needed to represent the dMRI data. Thus, by only discarding the pure-noise principal components in the image, the denoising does not affect the details or edges in the resulting image [5]. However, it is essential that the denoising method for IVIM ensures that no true signal is eliminated during the denoising process, thus this method needs to be tested before acceptance.

3.7 Between-volumes motion correction

Between-volumes motion refers to the misalginment of voxels between subsequent image acquisitions. To extract information about diffusion from dMRI, several identical images with different diffusion weighting are needed. Consequently, motion between these images can lead to inaccurate estimations, when one voxel in the first images does not correspond to the same voxel in another image anatomically.

There are methods that predict how the scanned object should look. These can be used to correct the image. FSL's EDDY is such a program that can predict and correct the movement [15]. Other corrective approaches that have emerged are those that tracks the movement of a physical marker placed on the subject during the scan, making the correction in real time [16].

EDDY is designed for correcting dMRI data with large differences in b-values and multiple encoding directions per b-value, which is in contrast to the data used for IVIM. Tools like EDDY, may not be directly applicable to IVIM-data.

3.8 Within-volume motion correction

Within-volume motion is a movement during a single imaging experiment, which causes misaligment of slices in the volume. The result can often be seen as zigzag patterns across the volume [5].

To solve this for dMRI data FSL's EDDY can be used [15]. In a similar way to between-volumes motion, within-volume motion could be corrected for in IVIM-data if the algorithm is tweaked to fit lower b-values.

3.9 Eddy current-induced distortion correction

During image acquisition, the rapidly changing magnetic fields will induce eddy-currents in conductive materials, such as scanner components, implant components or the human body. These currents will generate a magnetic field, causing distortion in the image.

In IVIM and dMRI, EPI sequences are used, which makes these distortions almost unavoidable. There are solutions to this, such as FSL's EDDY, but as previously explained this solution currently only works for high b-values.

3.10 Outlier detection

An outlier is a signal that deviates greatly from the anticipated signal and, in the case of dMRI, does not describe diffusion well. Outliers have several potential sources, such as noise, movement, chemical shift and metal items in the body.

The simplest method for outlier correction is to manually remove apparent outliers and interpolate the missing values. FSL's tool EDDY has an integrated outlier detection algorithm, which replaces detected outliers with a non-parametric prediction. As previously mentioned, this tool is optimized for high b-values, but remains to be implemented on IVIM-data.

3.11 Susceptibility distortion correction

Magnetic susceptibility is the ability of any substance or tissue to become magnetized when subjected to an external magnetic field. Differences in magnetic susceptibility between tissues causes distortions in the main magnetic field. In the MRI image, this will appear as a signal void or pile-up, most noticeably at anatomical boundaries, such as between air, soft tissue and bone.

Solutions to overcome over susceptibility distortions for dMRI have been explored, such as conducting a non-linear registration to an anatomical image and deep learning techniques. Other methods include another FSL solution, namely TOPUP [17]. TOPUP

estimates the susceptibility-related distortions by using data from different phase encoding directions, which contains artifacts in different directions. TOPUP can also be used for IVIM-data. However to apply the correction it is recommended to use FSL's EDDY.

3.12 EPI Nyquist ghost correction

The term "Nyquist ghosting" refers to the appearance of faint copies of the imaged object along the field of view (FOV), which is a common artifact from EPI readout. EPI pulse sequences are formed of a train of echoes, one for each line of the k-space. When acquiring data from a single line in k-space, a readout gradient is used to cause dephasing along this direction. Every other echo is acquired with the reverse frequency encoding direction in k-space. The spins along the different readout directions will accumulate phase. In a perfect scenario where the echos in every other line in the k-space are mirrored (with the same magnitude of accumulated phase), every other line can be flipped before reconstructing the image. However, this is not always the case as the adjacent lines in the k-space often accumulated different phase. This creates artifacts (ghosts) in the image with a shift of N/2 where N is the number of pixels in the FOV as the phase difference occurs between every other line.

Fundamentally, Nyquist ghosts occur when there is phase inconsistency between k-space lines. Many factors can contribute to Nyquist ghosting, including poor shimming, gradient coil heating, movement of subject, reconstruction errors and eddy currents. The ghosting effect is not limited to dMRI but appears in many MRI examinations.

Nyquist ghost correction is typically made during reconstruction. Solutions for IVIM exists, such as double sampling of the k-space, but at the cost of double scan time [18].

3.13 Gradient deviations: Gradient nonlinearities & gradient miscalibration

An ideal image read-out gradient will vary linearly with the distance from isocenter. However, to minimize peripheral nerve stimulations the linearity is commonly restricted to smaller FOVs, causing gradient nonlinearities further from the center. Additionally, gradient systems can differ between manufacturers and will be accomodated by a calibration process upon installation. In case of a miscalibration, geometric distortions may appear in the image. Correcting for the deviations in the gradient fields often leads to a blurring effect. If not corrected, gradient deviations can have an impact on the resulting b-value and may cause it to differ from the intended value for the sequence.

The foundation of the solutions for the gradient deviations are accurate characterization of the spatial variations. Phantoms with known dimensions or diffusion properties can be used for this [19]. There are other corrections methods that only corrects for the b-values. By measuring the ADC for a water phantom and compare with the calculated true diffusion coefficient a voxel-wise correction factor can be determined and used to

correct the deviation caused by gradients [20]. Although both corrections are based on high b-values, a similar approach, may be used for IVIM.

3.14 B_1 Bias field correction

The radiofrequency field (B_1) is not always uniform and can fluctuate significantly, resulting in a 15% variability in flip angle within a homogeneous area in the brain for 3T [21].

In dMRI, a typical way to eliminate this problem is to normalize against the b0-image. This is a very straightforward method, which cancels out the bias field and can be applied for IVIM. However, this may become a concern when normalization against the b0-image is not desired. For those situations a solution for dMRI could be to use FSL's FAST [22]. This approach estimates the bias field using adaptive low-pass filtering.

B_1 bias field correction have not been given much attention as a preprocessing step for dMRI, since the problem has been solved by normalization against b0-image. There are however, software packages such as FSL's that takes the bias field correction into account. For dMRI analysis, this step is more of an option than a necessity, provided that strong head motion and high magnetic field strengths are absent. Depending on situation the B_1 field correction might be relevant IVIM, for example when analyzing data with multiple echo times.

3.15 Spatial normalization

Manual structural segmentation in MRI images allows for labeling, localization, and quantification of local response. However, for larger studies, this manual procedure takes a long time and may introduces intra- and interobserver variability. Thus, for automatic labeling of anatomical MRI images, spatial normalization algorithms are an effective alternative.

dMRI data has a higher dimensionality compared to conventional MRI, which has created the need for special solutions [5]. To increase the sensitivity, objectivity, and interpretability of analysis of multi-subject diffusion imaging investigations, the FSL package includes a nonlinear registration method called tract-based-spatial statistics (TBSS) [23]. TBSS can adjust for misalignments among subjects in a population. The tool has become the gold standard for analysing dMRI data. A more specific registration method for dMRI is the Diffusion Tensor Imaging ToolKit (DTI-TK) [24]. This toolkit considers both anisotropic information and the estimated principal diffusion direction during spatial registration. Yet another method is Diffeomorphic Registration for Tensor Accurate alignMent of Anatomical Structures (DR-TAMAS), which uses the diffusion tensor for registration [25].

Given that IVIM is a form of dMRI, the similar techniques for spatial normalization for dMRI that can be applied to IVIM.

3.16 Summary

In their article, Tax et al. highlight the tools available for dMRI, although only a subset of these can be applied to IVIM-datasets [5]. At this present time, tools for the following preprocessing steps are directly applicable for IVIM: Brain extraction, Susceptibility distortion correction, EPI Nyquist ghost correction and Spatial normalization. On the other hand, there are other tools available that can be directly applied but require evaluation of the effect, such as signal drift correction and denoising methods.

The article also emphasizes the lack of standardization and accuracy metrics in the preprocessing steps and tools for dMRI, making it essential to specify the processing method and tool used. Tax et al. suggest combining and integrating multiple steps, including acquisition and reconstruction, to reduce the number of preprocessing steps. However, there is currently no consensus on the optimal preprocessing pipeline for neither dMRI nor IVIM-datasets, and the required steps may vary depending on the data.

To accurately correct data, it is important to have a thorough understanding of the data and the desired result, but this can be challenging if the characteristics of the data are unknown. Standardization may help to simplify the process, but this has yet to be adopted. Adopting standardized protocols and preprocessing tools may improve reproducibility and increase the reliability of results.

4

Signal drift correction

To obtain robust Intravoxel incoherent motion (IVIM) parameters, there is need to ensure that the observed signal decay is not influenced by confounding factors such as signal drift. In the presence of signal drift, an overestimation or an underestimation of the signal decay will be measured, leading to inaccurate results for the IVIM parameters. Hence, there is an interest to measure and correct for this signal drift. This chapter describes two correction methods: a temporal correction and a spatio-temporal correction, aimed at addressing the signal drift.

4.1 Introduction

IVIM is the model used to quantify and differentiate the diffusion and perfusion effects seen in diffusion-weighted MR images at lower b-values (b<1000 s/mm^2). Among the diffusion characteristics, the IVIM model provides an estimate of the perfusion fraction f, which describes the portion of the total signal decay due to perfusion. Accurate parameter estimation in diffusion-weighted imaging relies on the availability of high-quality data. However, these images are prone to artifacts, and the perfusion signal, which constitutes a small percentage of the total signal, can be particularly susceptible to these distortions.

When using IVIM to image perfusion small signal changes are of interest. One artifact that can disturb the data is signal drift. To investigate signal drift in this thesis, the pixel values for all non-diffusion-weighted images (b0-images) were extracted for each scan and subject and tracked over time. The signal from the b0-images should be unchanged regardless of when they were acquired and systematic deviations from this is what defines signal drift.

Occurrence of signal drift in dMRI has been previously reported and correction methods have been proposed. Vos et al. investigated the presence of signal drift in b0-images in a series of diffusion-weighted images [4]. The results showed a 5-6% drift in signal over a 15-minute scan session, with a quadratic effect over time. This led to the proposition of a temporal correction built on the assumption that the signal drift could be estimated with a quadratic fit. Hansen et al. expanded upon the previous research of Vos et al. and analyzed whether signal drift varied spatially in dMRI data [11]. The study found that signal drift did indeed vary spatially as well as temporally. This finding led to the proposal of a correction method that accounts for this spatial variation, namely spatio-temporal correction.

The secondary aim of this thesis was to investigate the occurrence of signal drift in diffusion-weighted imaging suitable for IVIM analysis at our lab in Sahlgrenska University Hospital and to evaluate the efficacy of correction methods using temporal and spatio-temporal approaches, as proposed by Vos et al. and Hansen et al., respectively. The effect of these correction methods on the perfusion fraction was also examined.

4.2 Method

4.2.1 MRI aqcuisition

MR data from six healthy volunteers were acquired on a 3T MR scanner (MR7700, Philips Healthcare, Best, the Netherlands) using a 32 channel head coil (same vendor). Three different scan protocols were used in the project: (1) three b-values (sIVIM), (2) 10 b-values (IVIM-10b) and (3) a flow-compensating/non-flow-compensating (IVIM-FC/NC) sequence with seven b-values.

Each volunteer was first scanned with a sequence (run 1) followed by a background scan of six b0-images. After the background scan the imaging was repeated (run 2) to estimate reproducibility. This procedure was done for all scans. The protocols were scanned in the following order: sIVIM, IVIM-10b, IVIM-FC/NC.

For all protocols, the following settings were utilized: echo time = 80 ms, repetition time = 3700 ms and the voxel size was $2 \times 2 \times 4$ mm^3. For the sIVIM scan, the b-values used were 0, 200, 800 [s/mm^2]. In the case of IVIM-10b, they were 0, 800, 5, 500, 10, 200, 20, 100, 30, 50 [s/mm^2]. For the IVIM-FC/IVIM-NC scan, the b-values used were 0, 200, 5, 100, 10, 30, 20 [s/mm^2]. Note that the b-values are listed in the order in which they were acquired and each b-value was acquired using six diffusion encoding directions (sides of a cube). No Dynamic Stabilization (updating center of frequency) was performed for any of the acquired volumes.

The project is part of a larger ethically approved project for the development of MR methods (entry no 2020-00029, PI Isabella Björkman-Burtscher). Collection of data for this project was approved by the Radiology Research Council.

4.2.2 Brain extraction and ROI

After the MRI acquisition, a brain mask was created for each protocol and volunteer using the BET tool [8]. This allowed for the analysis of brain tissue exclusively.

To study the temporal and spatio-temporal signal drift corrections in chapter 4.3.2, four regions of interest (ROIs) were chosen in homogeneous white matter in the brain. The ROIs were manually drawn for each subject using ITK-Snap [26]. The shapes and sizes of the regions differed for each subject but were comparable across the whole group. Figure 4.1 illustrates the different regions from one volunteer. The regions were divided into: anterior-left (A-L), anterior-right (A-R), posterior-left (P-L), and posterior-right (P-R).

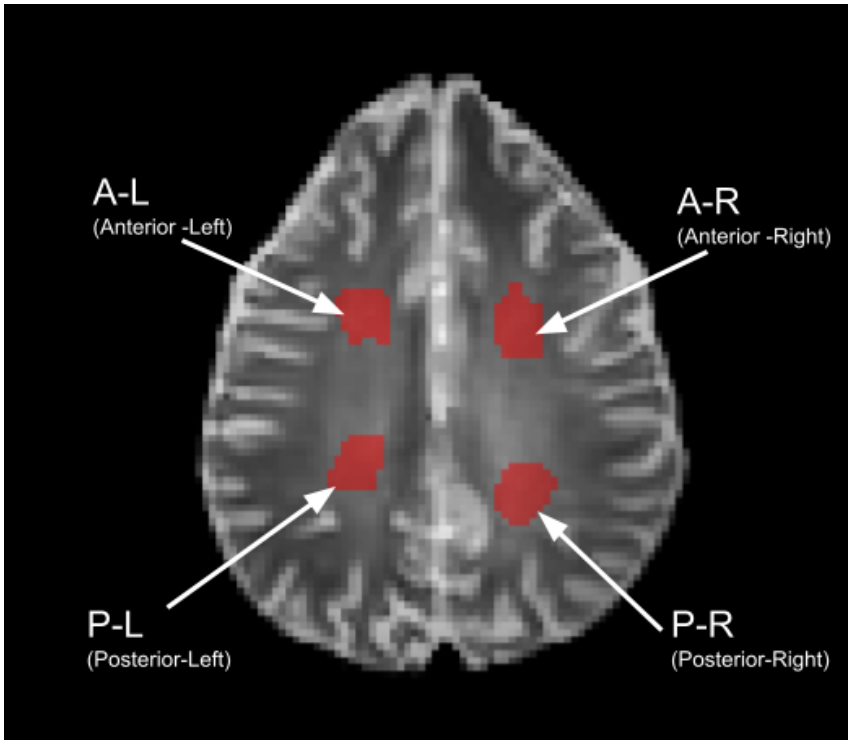

Figure 4.1: The figure shows shows an axial image slice of the brain of a volunteer where the ROIs are manually drawn in red. These four regions of white matter were used to analyze signal drift correction. The regions were defined as: Anterior-Left (A-L), Anterior-Right (A-R), Posterior-Left (P-L) and Posterior-Right (P-R).

4.2.3 Temporal correction

The temporal correction suggested by Vos et al. is a global correction and used for correcting the signal drift with respect to time [4]. The signal drift was estimated by a quadratic fit of the mean pixel value from the b0-images with the following expression,

$$S(n) = n^2 \cdot d_1 + n \cdot d_2 + s_0, \tag{4.1}$$

$S(n)$ is the mean pixel value in the uncorrected image n, d_1 and d_2 are the signal drift coefficients found through the fitting. s_0 is the signal offset at n=0.

Using equation 4.1, the corrected signal is given by,

$$S_{corrected} = \frac{S(n)}{(n^2 \cdot d) + (n \cdot d_2) + s_0} \cdot 100 \tag{4.2}$$

where $S_{corrected}$ is the corrected signal normalized to 100. The temporal correction in equation 4.2 was applied to all diffusion weighted images. Note that this is a global correction, thus the same correction was applied on every voxel.

4.2.4 Spatio-temporal correction

The spatio-temporal correction is an expansion of the temporal correction at voxel level with respect to spatially fluctuating signal drift [11]. Uncorrected b0 image data were used to fit the model,

$$V(X,n) = B_T(X,n) + B_{TSv}(X,n) + B_{TSn}(X,n) + B_{TSn^2}(X,n) + v_{0,x} \tag{4.3}$$

where X is a vector containing the x, y, z coordinates for the given voxel and n is the image index. $B_T(X,n), B_{TSv}(X,n), B_{TSn}(X,n)$ and $B_{TSn^2}(X,n)$ are polynomials. For the whole expansion please see appendix A.1. The spatio-temporal corrected signal is then given by,

$$\hat{V}(X,n) = \frac{V(X,n)}{B_T(X,n) + B_{TSv}(X,n) + B_{TSn}(X,n) + B_{TSn^2}(X,n) + v_{0,x}} \cdot 100 \tag{4.4}$$

The correction was applied to all diffusion-weighted images.

4.2.5 Parameter maps computation

In order to investigate how the perfusion fraction varied with the signal drift and the corrections, parameter maps were reconstructed. Depending on the scan protocol, different models were utilized to describe the signal decay. For sIVIM, the signal decay was fitted with following model,

$$\frac{S(b)}{S(0)} = (1-f)e^{-bD_{tissue}} + f\delta(b) \tag{4.5}$$

where f is the perfusion fraction, D_{tissue} is the tissue diffusion coefficient. $\delta(b)$ is the dirac delta function.

The model used for IVIM-10b was,

$$\frac{S(b)}{S(0)} = (1-f)e^{-bD_{tissue}} + fe^{-bD^*} \tag{4.6}$$

For the IVIM-FC/NC, the signal decay is given by,

$$\frac{S(b,\alpha)}{S(0)} = (1-f)e^{-bD_{tissue}} + fe^{-bD_{blood}}e^{-\alpha^2 v_d^2} \tag{4.7}$$

where α is the flow-weighting factor and v_d is the velocity dispersion and D_{blood} is the diffusion coefficient of blood ($1.75\mu m^2/ms$). Furthermore, the images for IVIM-FC and IVIM-NC were combined into one image before computing the parameter maps according to the model.

The perfusion fraction was investigated by averaging f over region A-L described in figure 4.1, for each scan protocol. To investigate how the temporal and spatio-temporal corrections affected the perfusion fraction, the result was normalized to the uncorrected data.

4.3 Results

The results in chapter 4.3.1 and 4.3.2 contain results from two of the six volunteers, volunteers A and B, which were acquired on different days. The results from volunteer A are representative of five of the volunteers, while the results from volunteer B showed a deviation. The results from all volunteers can be found in appendix A.2.

4.3.1 Temporal correction

For the temporal correction, the signal drift was estimated using a global mean pixel value of each b0-image. Each global value was normalized to the first acquired b0-image. The signal drift was then estimated by quadratric model fitting (equation 4.1). Finally, the fitted model was applied to correct the data for temporal signal drift. Figures 4.2-4.5 shows the uncorrected, as well as the corrected data for volunteer A, for the four scanned protocols. Similarly, figures 4.6-4.9 shows uncorrected as well as corrected data for volunteer B.

Figure 4.2 reveals a trend of increasing signal over time for run 1, and subsequently decreasing signal over time for run 2 for sIVIM. The maximal signal drift in uncorrected data for this protocol was 0.60% (run 1) and 1.18% (run 2). The maximal signal drift remaining in the temporally corrected data for sIVIM was 0.29% (run 1) and 0.25% (run 2), see figure 4.2.

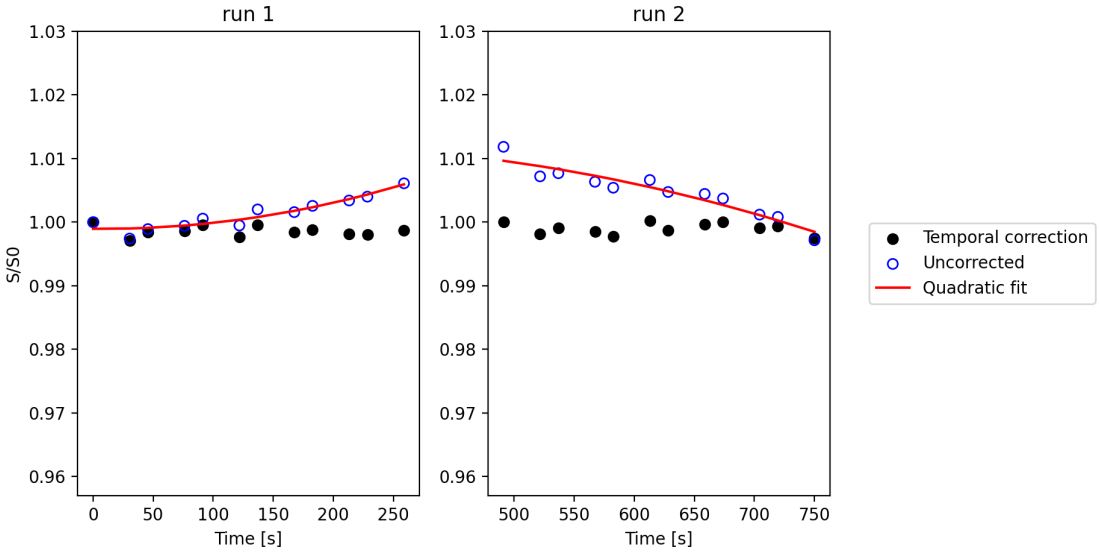

Figure 4.2: The uncorrected and temporally corrected average pixel value for the entire brain, from sIVIM of volunteer A. The uncorrected b0-signal showed an increasing signal drift during run 1 (left), followed by a decrease during run 2 (right). The temporal correction was applied using the quadratic fit of the uncorrected data. Note that the uncorrected data is normalized to the first b0-image from run 1.

For IVIM-10b, the signal decreased with time during both runs, as shown in figure 4.3. The maximal signal drift in uncorrected data was 4.05% (run 1) and 3.74% (run 2). The maximal signal drift for the temporally corrected data was 0.18% (run 1) and 0.17% (run 2) for IVIM-10b.

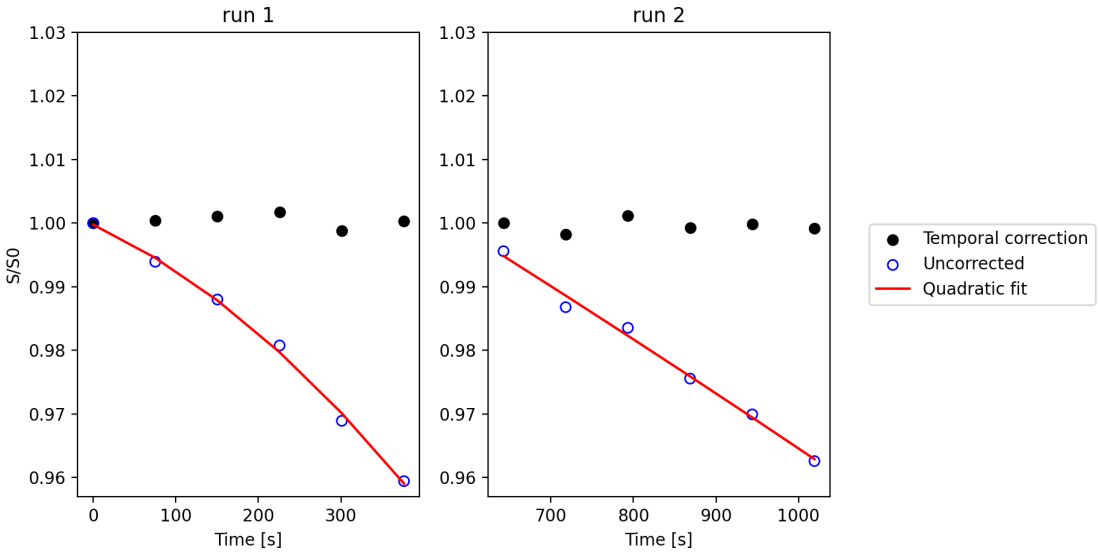

Figure 4.3: The uncorrected and temporally corrected average pixel value for the entire brain, from IVIM-10b of volunteer A. The uncorrected b0-signal showed decreasing signal in both runs, view run 1 (left) and run 2 (right). The temporal correction was applied using the quadratic fit of the uncorrected data. Note that the uncorrected data is normalized to the first b0-image from run 1.

For the flow-compensated scan IVIM-FC, the signal drift during run 1 increases with time, with a maximum loss of 2.02% observed, see figure 4.4. The second run, on the other hand, does not follow the same pattern with maximum signal drift of 0.27 %. The maximal signal drift in the temporally corrected data was 0.12% (run 1) and 0.15% (run 2).

Although both IVIM-FC (figure 4.4) and IVIM-NC (figure 4.5) use the same b-values, a difference in trends of the signal drift can be observed. For IVIM-NC, the signal drift is larger for the second run compared to the first whilst opposite can be observed for IVIM-FC. The maximal signal drift observed in uncorrected data for IVIM-NC was 0.41% (run 1) and 1.05% (run 2). The maximal signal drift for the temporally corrected data was 0.20% (run 1) and 0.24% (run 2).

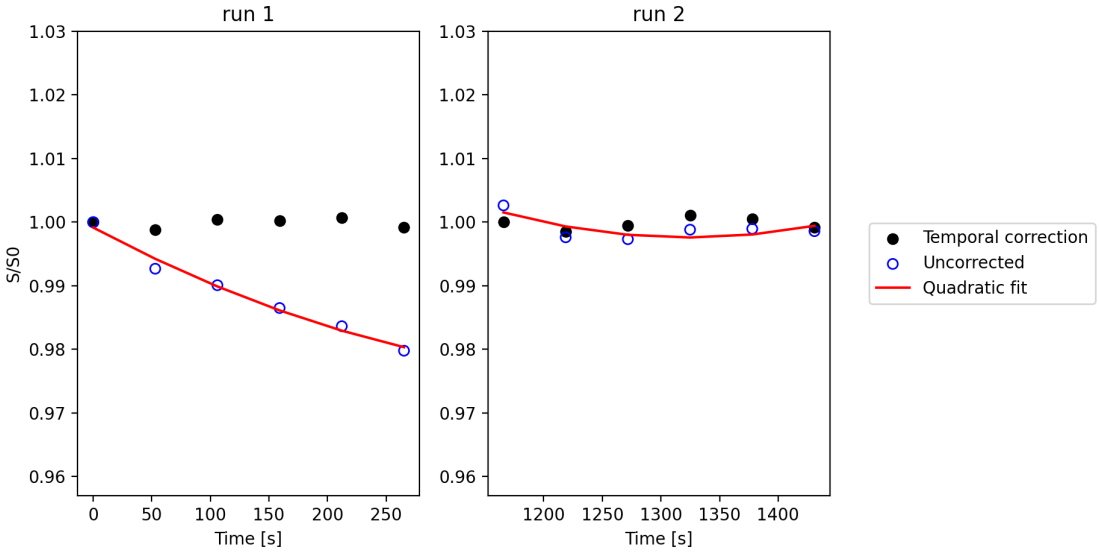

Figure 4.4: The uncorrected and temporally corrected average pixel value for the entire brain, from IVIM-FC of volunteer A. The uncorrected b0-signal showed a clear signal decrease in run1 (left) and less evident signal decrease in run 2 (right). The temporal correction was applied using the quadratic fit of the uncorrected data. Note that the uncorrected data is normalized to the first b0-image from run 1.

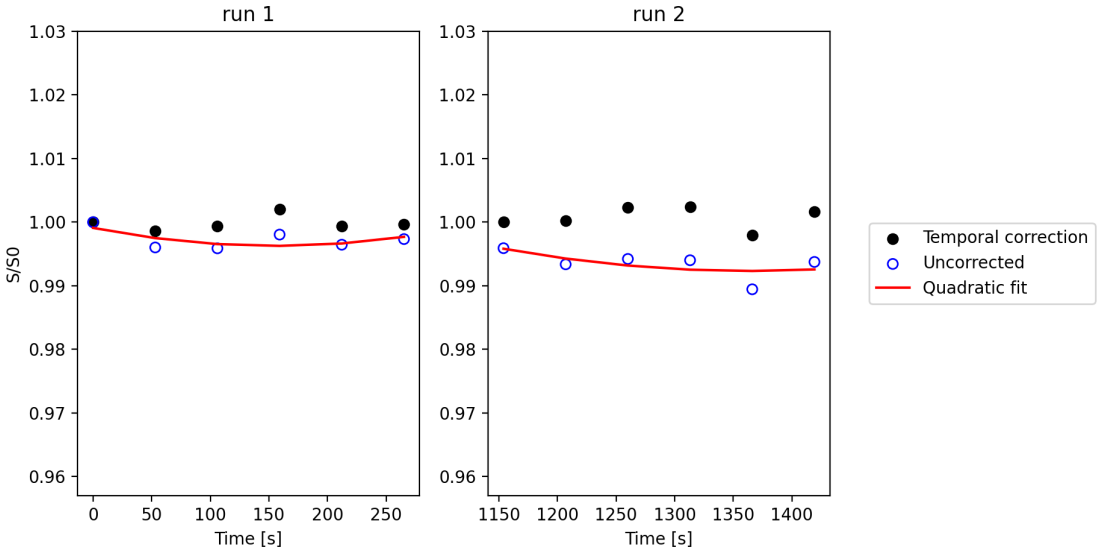

Figure 4.5: The uncorrected and temporally corrected average pixel value for the entire brain, from IVIM-NC of volunteer A. The uncorrected b0-signal showed a minimal signal decrease run1 (left) and a more evident signal decrease in run 2 (right). The temporal correction was applied using the quadratic fit of the uncorrected data. Note that the uncorrected data is normalized to the first b0-image from run 1.

The data shown in figures 4.6-4.9 were acquired on a different day and a different volunteer than the data in figures 4.2-4.5. Figures 4.6 and 4.7 provide an example of when the mean

pixel values of the b0-images have a wider dispersion and cannot be approximated with the quadratic fit. This is true for run 1 in both figures. It should be noted, however, that these deviating results were not observed in the other volunteers.

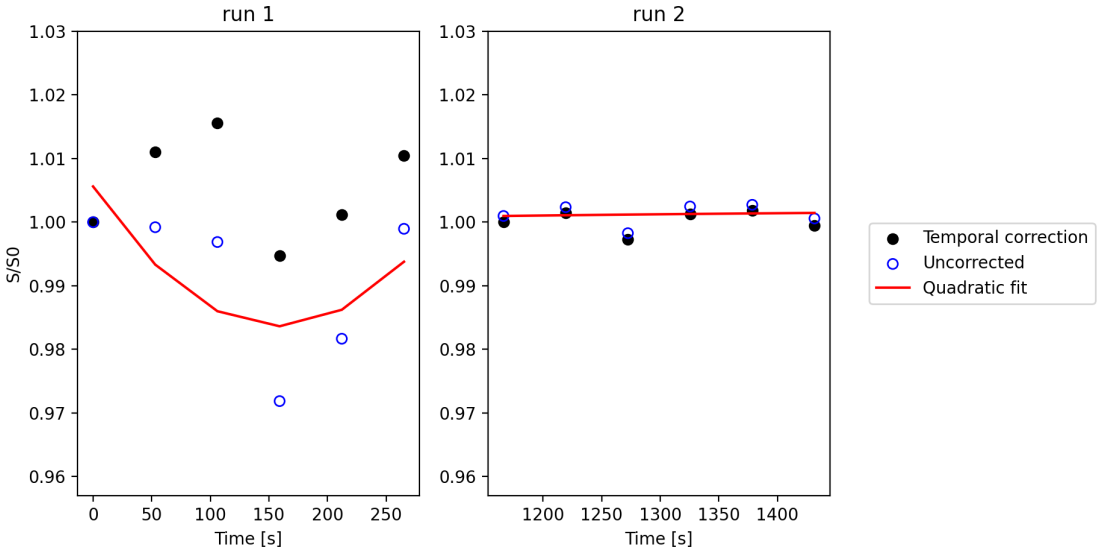

Figure 4.6: The uncorrected and temporally corrected average pixel value for the entire brain, from IVIM-FC of volunteer B. The uncorrected b0-signal showed a bigger spread in signal drift for run 1 (left) and minimal signal drift for run 2 (right). Note that the uncorrected data is normalized to the first b0-image from run 1.

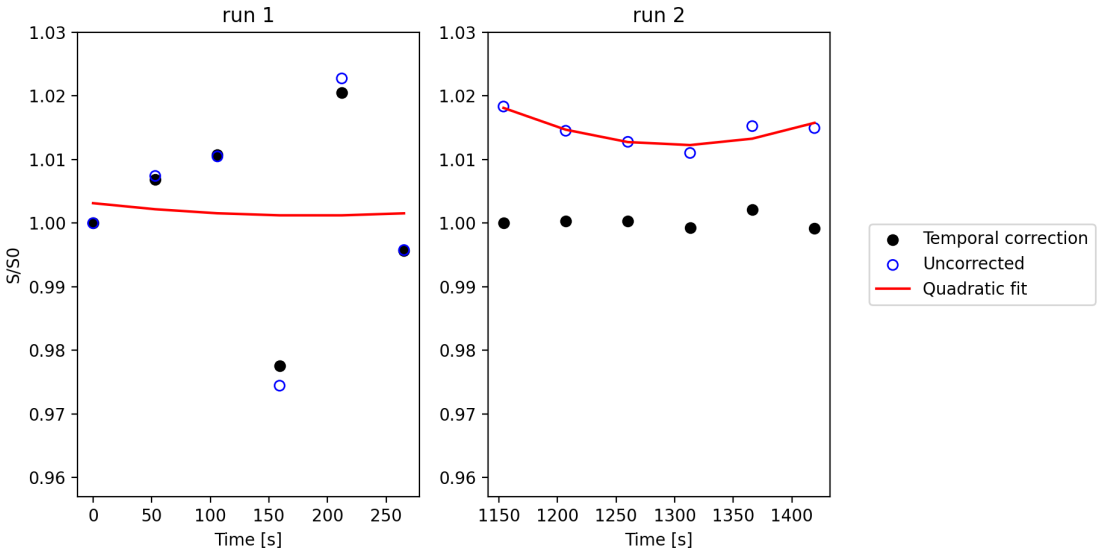

Figure 4.7: The uncorrected and temporally corrected average pixel value for the entire brain, from IVIM-NC of volunteer B. The data showed an anomaly with a larger spread of the signal drift in the b0-images for run 1 (left). Note that the uncorrected data is normalized to the first b0-image from run 1.

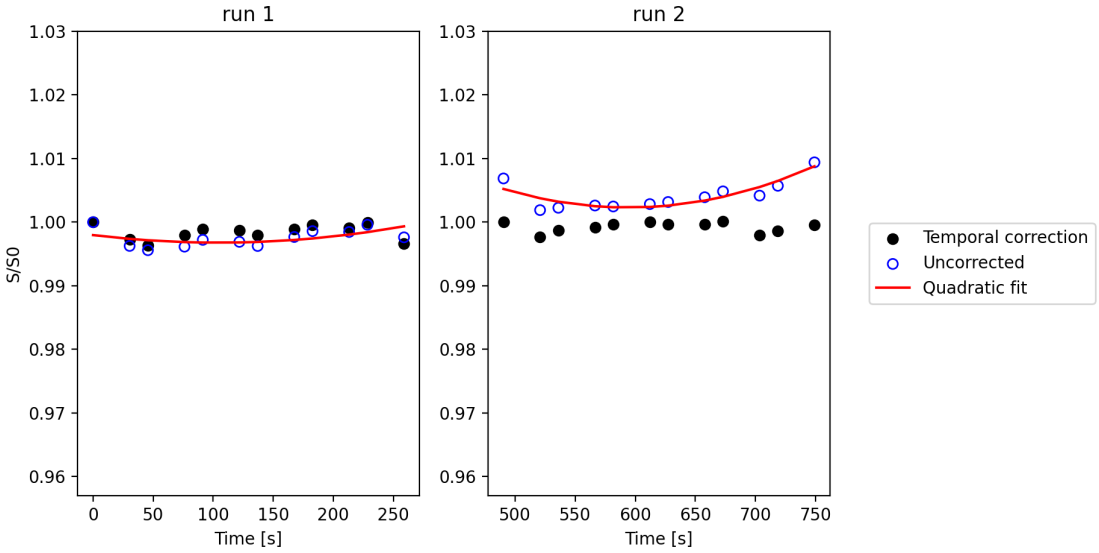

Figure 4.8: The uncorrected and temporally corrected average pixel value for the entire brain, from sIVIM of volunteer B. The uncorrected b0-signal showed a minimal signal drift during run 1 (left) and an increase in signal during run 2 (right). Note that the uncorrected data is normalized to the first b0-image from run 1.

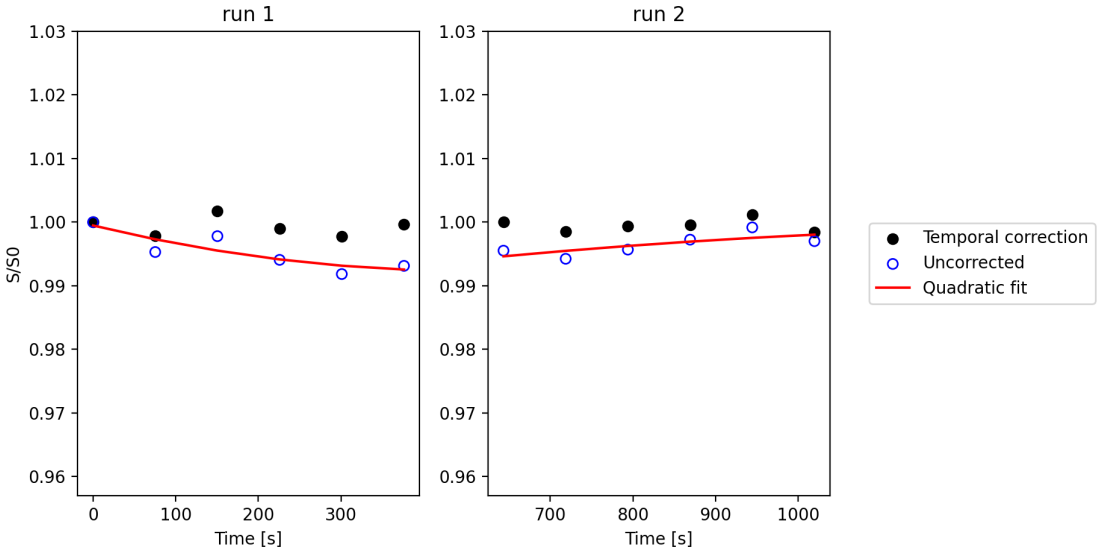

Figure 4.9: The uncorrected and temporally corrected average pixel value for the entire brain, from IVIM-10b of volunteer B. The uncorrected b0-signal showed a decrease in signal during run1 (left) and an increase during run 2 (right). Note that the uncorrected data is normalized to the first b0-image from run 1.

The signal drift for sIVIM (figure 4.8), shows a minimal signal drift during run 1 and an increase in signal magnitude for run 2. In the case of IVIM-10b in figure 4.9 the signal drift does not exhibit the strong negative signal drift observed in other volunteers for the same protocol.

4.3.2 Spatio-temporal correction

In order to evaluate the effectiveness of spatio-temporal correction, which takes into account both spatial and temporal variations of the signal, four different regions of white matter as defined in figure 4.1 were studied. The mean pixel values from b0-images in these regions were used to visualize the signal drift in uncorrected and corrected data. As before, the signal drift is defined as the change in the mean pixel value of the b0-images over time, compared to the initial image in the sequence i.e. the first b0-image in run 1 for each scans sequence. To compare the performance of spatio-temporal correction with the temporal correction, both results are displayed on the same graph. The data in this section were mainly collected from volunteers A and B which were acquired on different days. Additionally, the mean and standard deviation of the relative signal drift was calculated for the whole group in order to give a comprehensive overview of the temporal and spatio-temporal correction methods.

To evaluate the mean signal drift of a given region, the mean pixel values of consecutive b0-images were normalized to the first b0-image obtained in the first run (run 1) of each volunteer and scan sequence. The group average of the signal drift and its standard deviation for each scan sequence were then calculated using the mean signal drift obtained from the two runs (run 1 and run 2) of the four ROIs in the brain (A-L, A-R, P-L and P-R) from all six volunteers, see table 4.1.

Table 4.1: The group average signal drift, ($\bar{S}$), from both runs (run 1 and run 2) of the combined regions (A-L, A-R, P-L and P-R) and their standard deviation for the six volunteers. The signal drift is calculated as the ratio between the group average mean pixel value of the consecutive b0-images and the group average mean pixel value of the initial b0-image (run 1) for each scan sequence and.

	$\bar{S}_{\text{Uncorrected}} \pm$ std	$\bar{S}_{\text{Temporal correction}} \pm$ std	$\bar{S}_{\text{Spatio-temporal correction}} \pm$ std
sIVIM	1.000 ± 0.007	1.001 ± 0.006	1.000 ± 0.010
IVIM-10b	0.989 ± 0.014	0.998 ± 0.010	1.007 ± 0.029
IVIM-FC	0.998 ± 0.007	1.002 ± 0.007	0.998 ± 0.009
IVIM-NC	1.000 ± 0.006	1.002 ± 0.006	0.999 ± 0.008

Table 4.1 shows the average signal drift observed in the different protocols for all six volunteers. The mean value of the signal in uncorrected data for scan sIVIM and IVIM-NC indicate minor observable signal drift present for the whole population, while a decrease in the mean signal is observed for IVIM-10b and IVIM-FC. The maximal mean value of the signal was observed for, IVIM-10b, at 1.1% for the group.

For the sIVIM protocol, see figure 4.10, the maximal signal drift in the uncorrected data is 2.78% in region A-R (run 2). The maximal drift in spatio-temporal corrected data is observed in region P-L (run 1) at 2.27%, where the maximal signal drift in uncorrected data was 1.97%. In comparison, the maximal signal drift within this region and run, was 1.27% for the temporal corrected data.

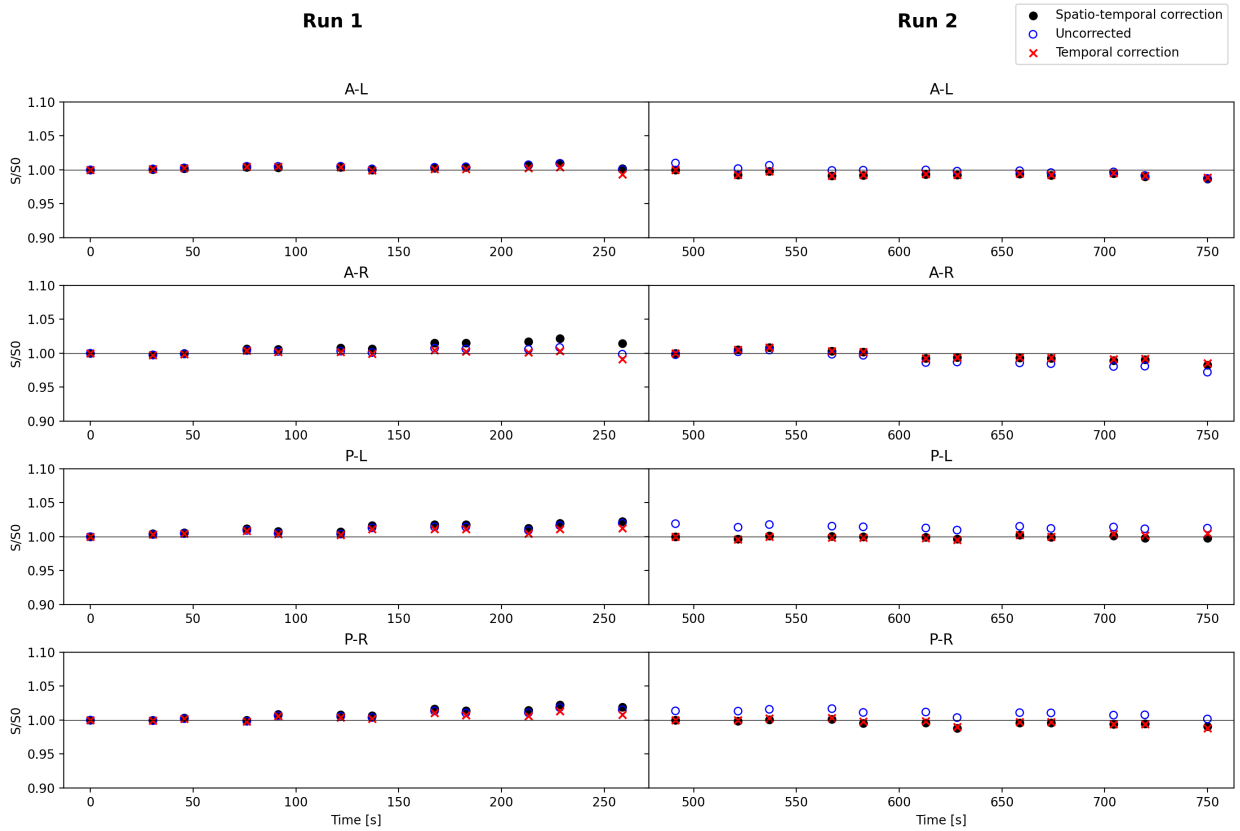

Figure 4.10: Uncorrected, temporal corrected and spatio-temporal corrected data from sIVIM, volunteer A, for the repeated scans run 1 (left) and run 2 (right). The data for each row is the mean pixel values from each of the four respective regions: A-L, A-R, P-L, and P-R. Note all uncorrected data are normalized to the first b0 from run 1.

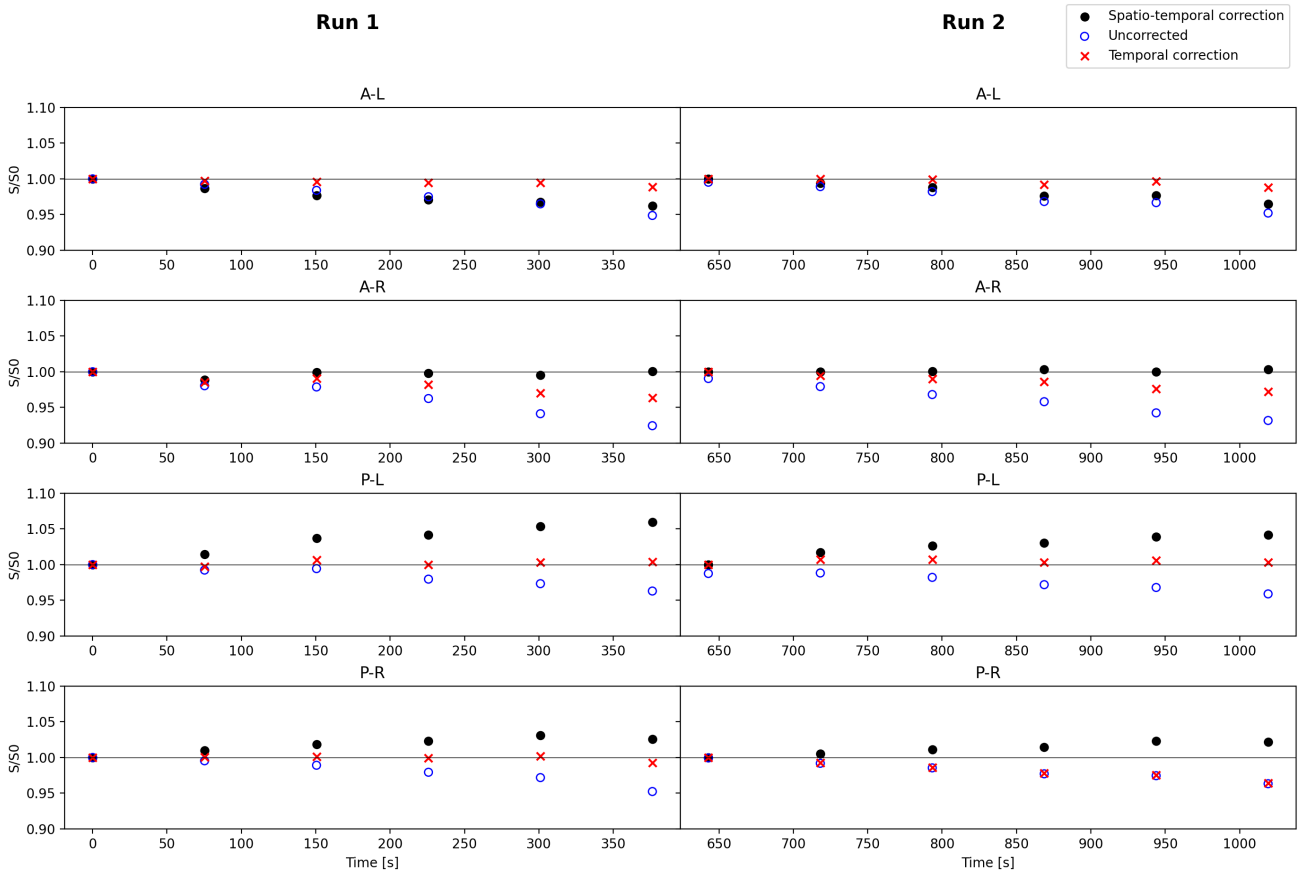

Figure 4.11: Uncorrected, temporal corrected and spatio-temporal corrected data from IVIM-10b, volunteer A, for the repeated scans run 1 (left) and run 2 (right). It should be noted that the temporal correction performs better at correcting for signal drift in this scan. The uncorrected signal was observed to decrease for both runs for all regions. The data for each row is the mean pixel value from each of the four distinct regions: A-L, A-R, P-L, and P-R. Note all uncorrected data are normalized to the first b0 from run 1.

For IVIM-10b in figure 4.11, a signal drift can be observed.IVIM-10b has a larger signal drift compared to the other scan protocols. The maximal signal drift in the uncorrected data was observed at 7.55% for A-R (run 1). The maximal signal drift observed in spatio-temporal corrected data was 5.96% in P-L (run 1), the signal drift in the uncorrected data in this scan and region was 3.96%. In comparison, the maximal signal drift measured in P-L (run 1) was 3.63% for temporal correction. It is worth noting that the regions of interest vary in shape, but are roughly equivalent in size.

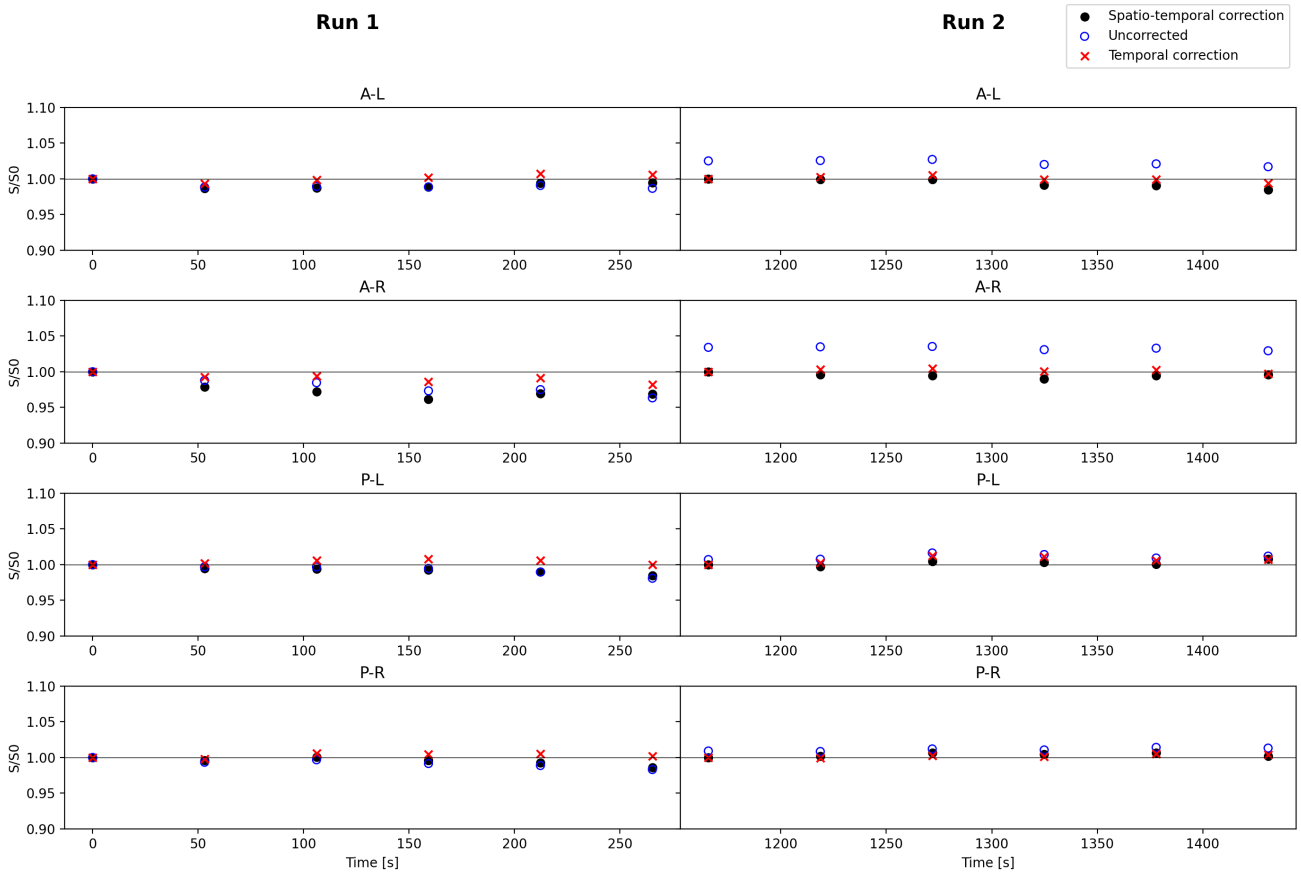

Figure 4.12: Uncorrected, temporal corrected and spatio-temporal corrected data from IVIM-FC, volunteer A, for the repeated scans run 1 (left) and run 2 (right). The data for each row is the mean pixel value from the four respective regions: A-L, A-R, P-L, and P-R. Note all uncorrected data are normalized to the first b0 from run 1.

For IVIM-FC (figure 4.12), the maximal signal drift in both uncorrected and spatio-temporal corrected data was observed in A-R (run 1), 3.66% and 3.83%, respectively. Note that the signal drift in the spatio-temporal corrected data is greater. On the other hand, the maximal signal drift observed in this region and run for temporally corrected data was 1.18%.

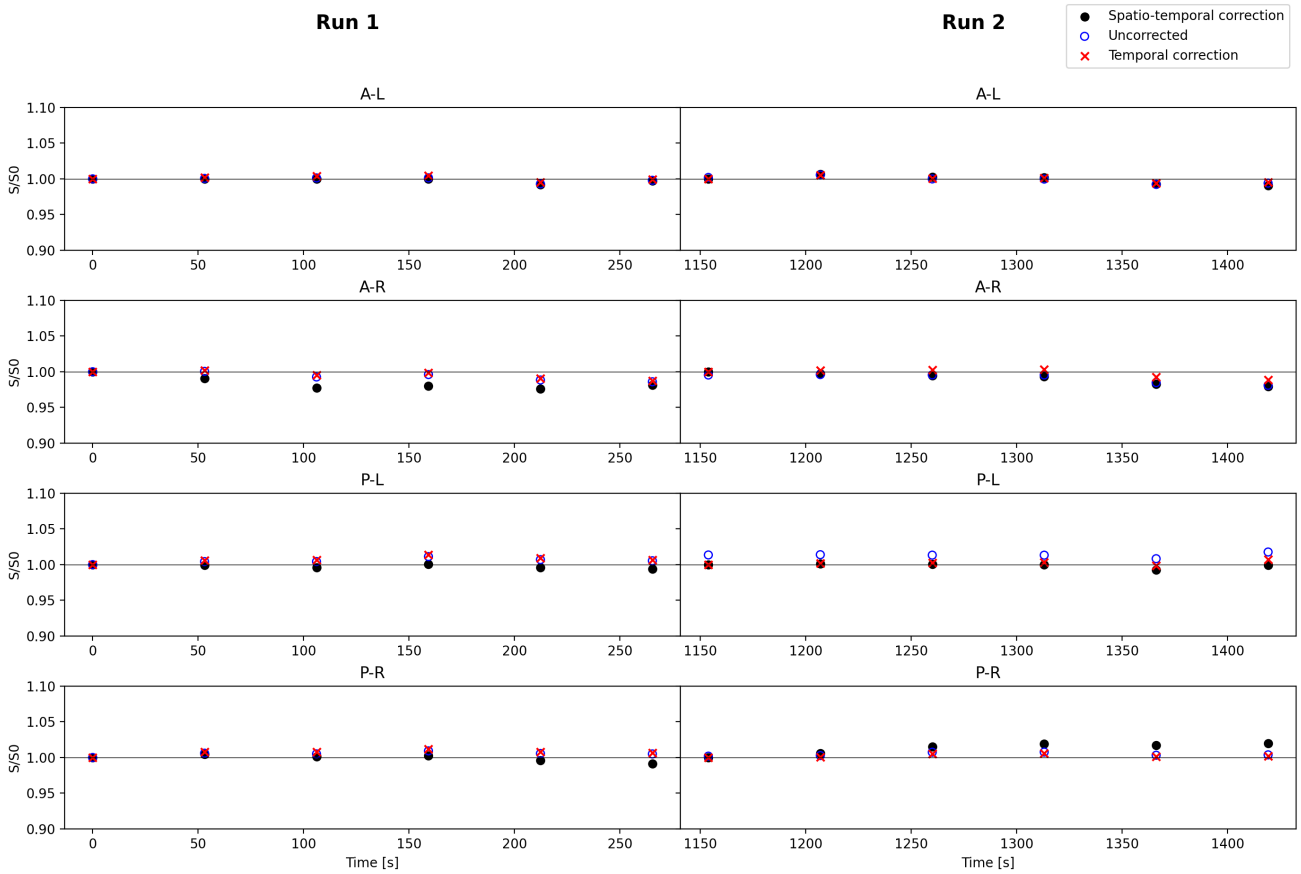

Figure 4.13: Uncorrected, temporal corrected and spatio-temporally corrected data from IVIM-NC, volunteer A, for the repeated scans run 1 (left) and run 2 (right). The data for each row is the mean pixel value from the four respective regions: A-L, A-R, P-L, and P-R. Note all uncorrected data are normalized to the first b0 from run 1.

Figure 4.13 shows that the uncorrected and corrected data points for region A-L nearly overlap. In contrast, the correction for region P-R (run 2) overestimates the signal drift, resulting in amplifying the drift rather than correct for it. The maximum signal drift in the uncorrected data was observed in region A-R (run 1) at 1.40%, while the maximum drift in the spatio-temporal corrected data within this region was 2.40%. However, for the temporal corrected data it was found to be 1.27%.

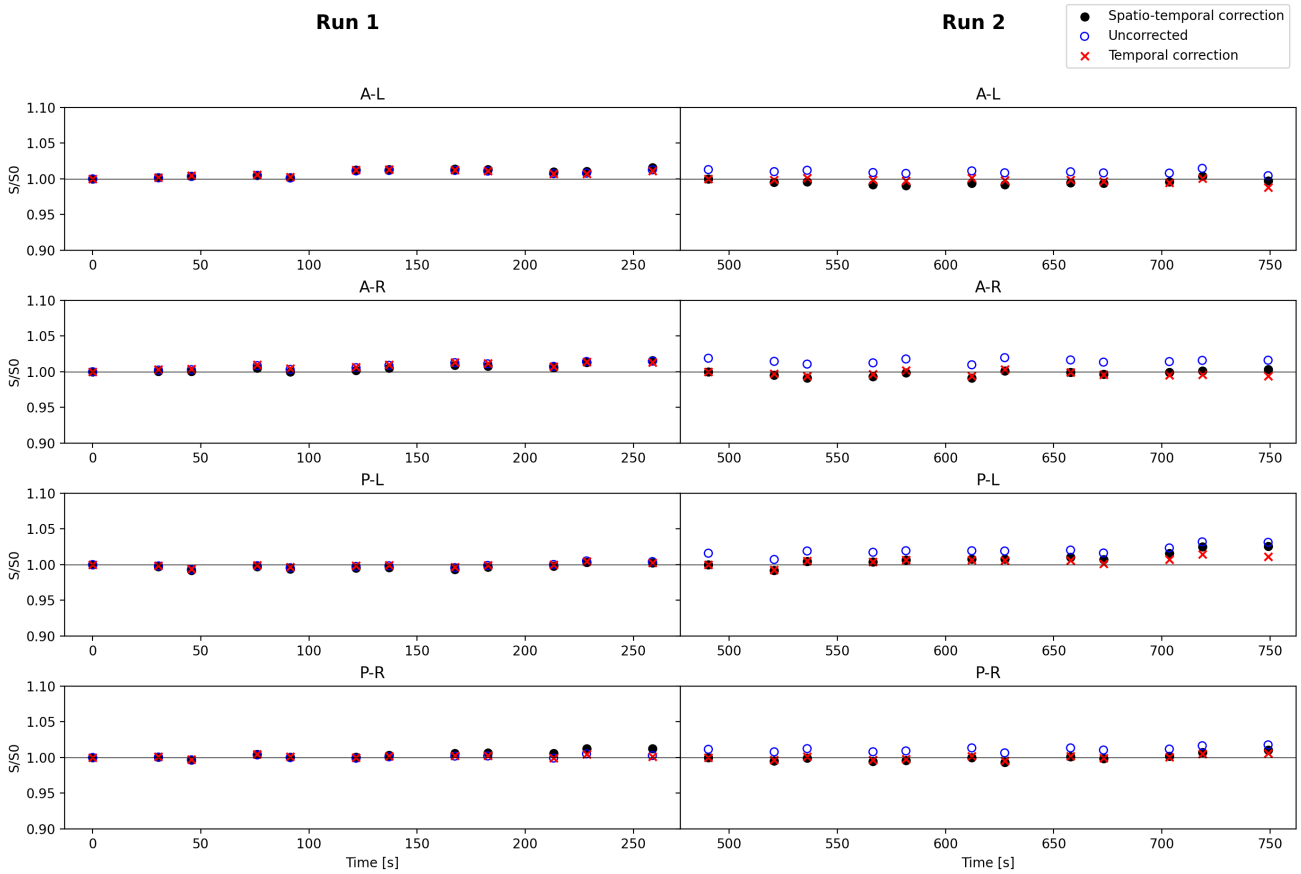

Figure 4.14: Uncorrected, temporal corrected and spatio-temporally corrected data from sIVIM, volunteer B, for the repeated scans run 1 (left) and run 2 (right). The data for each row is the mean pixel value from the four respective regions: A-L, A-R, P-L, and P-R. Note all uncorrected data are normalized to the first b0 from run 1.

For volunteer B in figure 4.14, the maximal signal drift was observed at 3.19% for region P-L (run 2). The signal drift in this region for the spatio-temporal corrected data was 2.60% and 1.44% for the temporal correction.

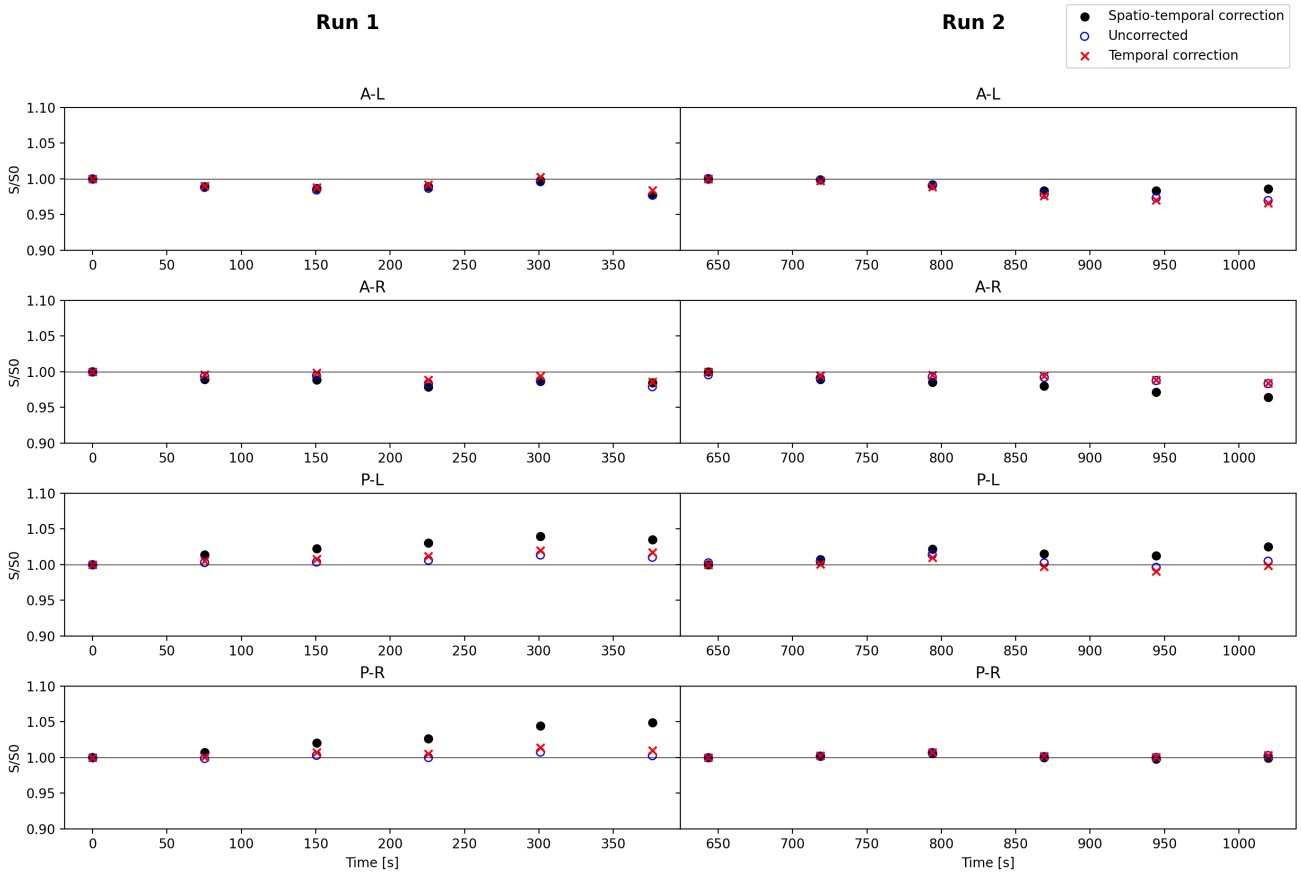

Figure 4.15: Uncorrected, temporal corrected and spatio-temporally corrected data from IVIM-10b, volunteer B, for the repeated scans run 1 (left) and run 2 (right). The data for each row is the mean pixel value from the four respective regions: A-L, A-R, P-L, and P-R. Note all uncorrected data are normalized to the first b0 from run 1.

The maximal signal drift observed for IVIM-10b, as shown in figure 4.15, was in region A-L (run 2) at 3.03% in the uncorrected data. By comparison, the maximal signal drift was 1.67% with spatio-temporal correction and 3.40% with temporal correction. It should be noted that spatio-temporal correction outperformed temporal correction in this instance.

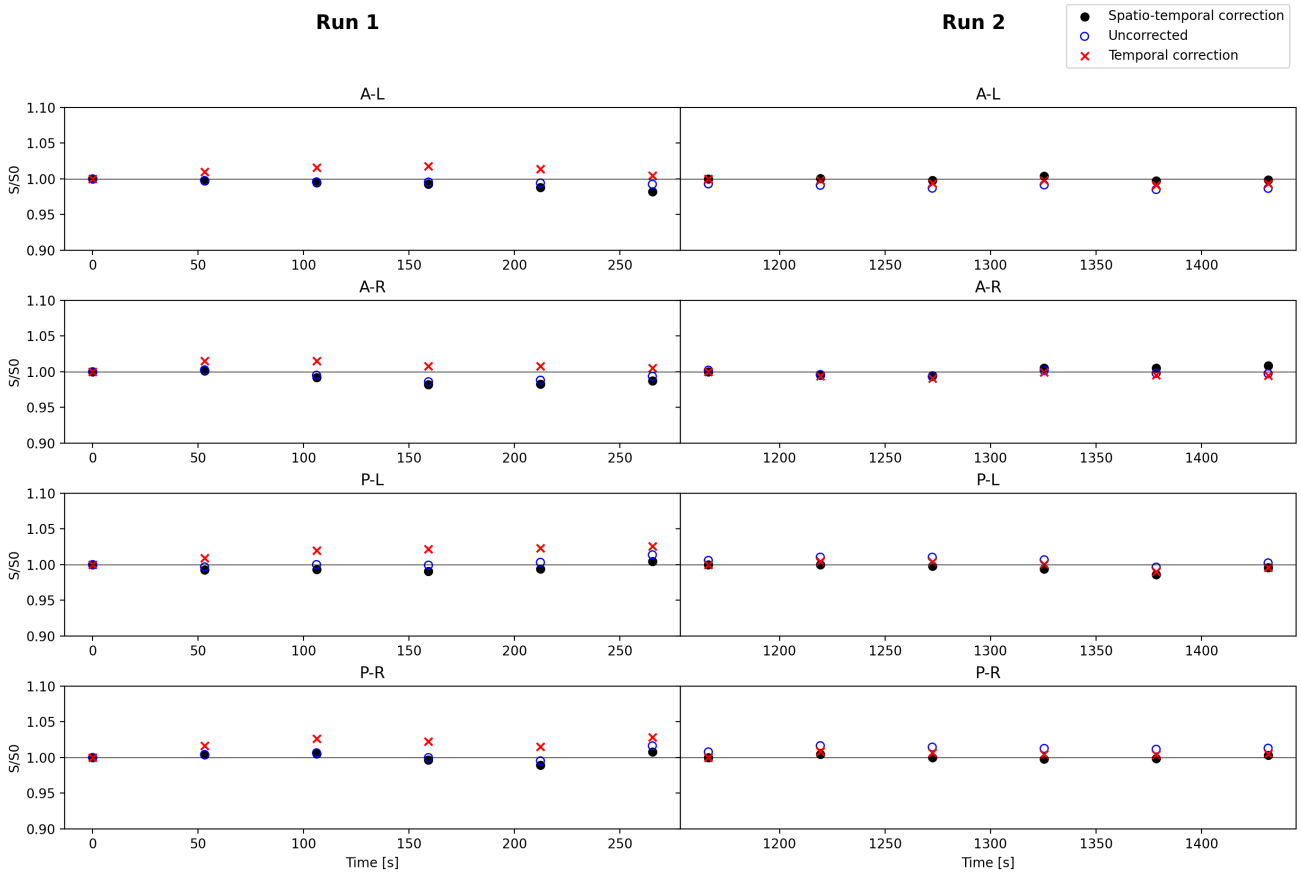

Figure 4.16: Uncorrected, temporal corrected and spatio-temporally corrected data from IVIM-FC, volunteer B, for the repeated scans run 1 (left) and run 2 (right). The data for each row is the mean pixel value from the four respective regions: A-L, A-R, P-L, and P-R. Note all uncorrected data are normalized to the first b0 from run 1.

For IVIM-FC in figure 4.16, the maximum signal drift in uncorrected data was 1.65% for region P-R (run 2). The maximum signal drift in spatio-temporal corrected data for this region and run was 0.44%, while the maximal signal drift in temporal correction was 0.86%. Note that the spatio-temporal correction yielded better results in this case.

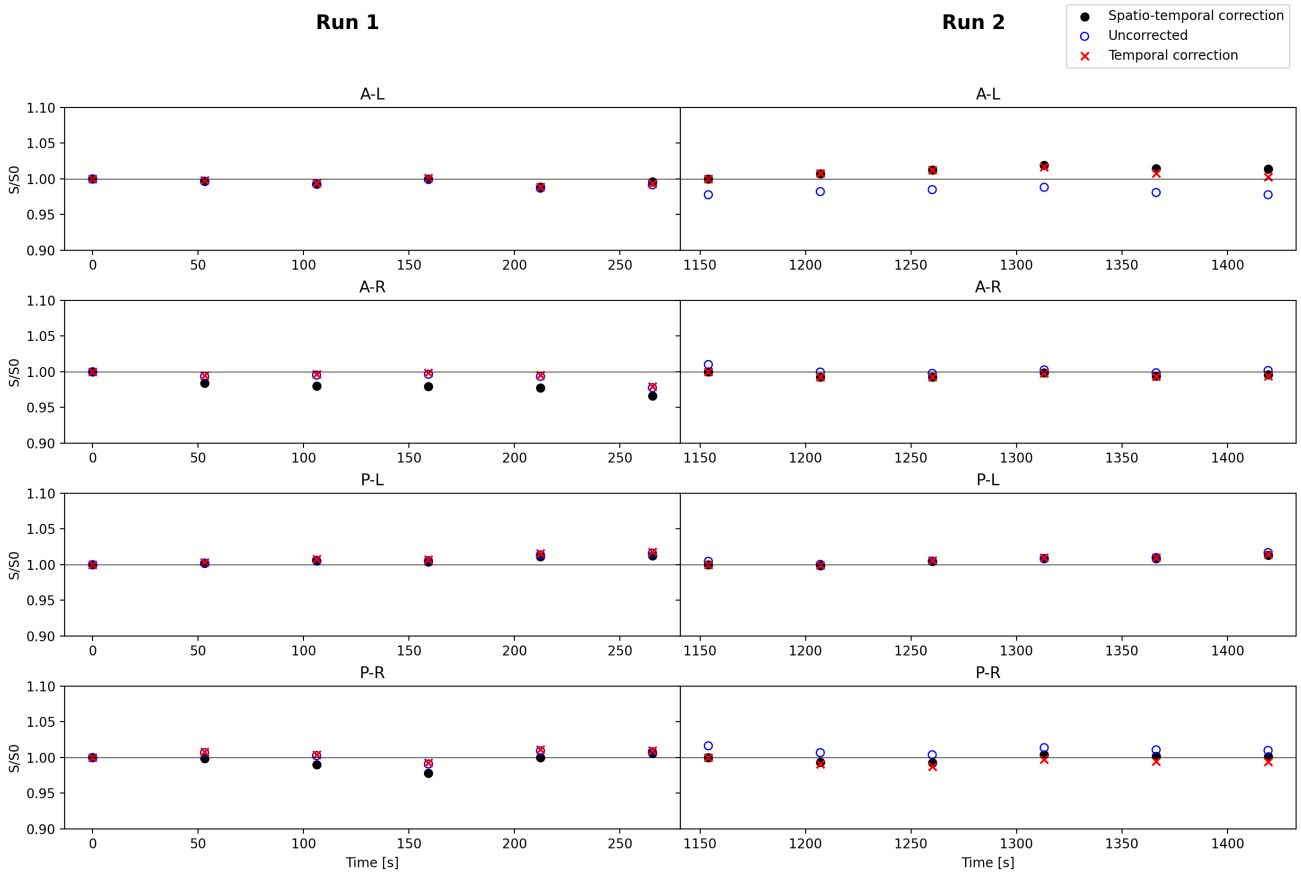

Figure 4.17: Uncorrected, temporal corrected and spatio-temporally corrected data from IVIM-NC, volunteer B, for the repeated scans run 1 (left) and run 2 (right). The data for each row is the mean valuefrom the four respective regions: A-L, A-R, P-L, and P-R. Note all uncorrected data are normalized to the first b0 from run 1.

For IVIM-FC in figure 4.17, the maximum signal drift in uncorrected data was observed in region A-R for run 1, at 2.24%. In contrast, the maximum signal drift in spatio-temporal corrected data was 3.36%. On the other hand, temporal correction resulted in a maximum signal drift of 2.08%, which was the best performance among the three methods for this protocol.

4.3.3 Perfusion fraction

This section examines the various results for the estimation of the perfusion fraction for the white matter in region A-L, using all six volunteers and protocols.

In table 4.2, the values of the uncorrected and corrected perfusion fraction for sIVIM are shown for all volunteers. For both temporal and spatio temporal correction, the maximum difference between corrected and uncorrected was observed for volunteer D at 0.43% and 0.98%, respectively. Overall, the differences between the uncorrected and corrected perfusion fractions were less than 1% for all volunteers.

Table 4.2: The mean value of the absolute perfusion fraction from sIVIM was calculated for uncorrected and corrected data, using the mean of perfusion fraction values from runs 1 and 2. The corrected value was normalized to the uncorrected value and presented as a percentage. This analysis was performed on all volunteers in region A-L

Volunteer	$f_{\text{Uncorrected}}$	$f_{\text{Temporal correction}}$ (%)	$f_{\text{Spatio-temporal correction}}$ (%)
A	3.330	3.336 (100.18)	3.316 (99.58)
B	3.134	3.124 (99.68)	3.107 (99,14)
C	3.201	3.209 (100.25)	3.222 (100,66)
D	3.051	3.064 (100.43)	3.081 (100.98)
E	3.371	3.375 (100.12)	3.371 (100.00)
F	3.243	3.237 (99.81)	3.256 (100,40)

The values of the uncorrected and corrected perfusion fraction for IVIM-10b are shown for all volunteers in table 4.3. For temporal correction, the maximum difference between the corrected and uncorrected perfusion fraction was observed for volunteer A at 11.57%. For spatio-temporal correction, the maximum difference was observed for volunteer C at 10.44%.

Table 4.3: The mean value of the absolute perfusion fraction from IVIM-10b was calculated for uncorrected and corrected data, using the mean of perfusion fraction values from runs 1 and 2. The corrected value was normalized to the uncorrected value and presented as a percentage. This analysis was performed on all volunteers in region A-L.

Volunteer	$f_{\text{Uncorrected}}$	$f_{\text{Temporal correction}}$ (%)	$f_{\text{Spatio-temporal correction}}$ (%)
A	3.406	3.012 (88.43)	3.240 (95.13)
B	3.228	3.206 (99.32)	3.127 (96.87)
C	3.466	3.172 (91.52)	3.104 (89.56)
D	3.412	3.126 (91.62)	3.125 (91.59)
E	3.908	3.699 (94.65)	4.20 (107.47)
F	3.763	3.597 (95.59)	3.723 (98.94)

Table 4.4 presents the values of the uncorrected and corrected perfusion fraction for IVIM-FC/NC for all volunteers. In this protocol, the corrected perfusion fraction deviates more from the uncorrected value compared to sIVIM and IVIM-10b. For temporal correction, the maximum difference between the corrected and uncorrected perfusion fraction was observed for volunteer A at 112.82%. For spatio-temporal correction, the maximum difference was observed for volunteer D at 46.80%.

Table 4.4: The mean value of the absolute perfusion fraction from IVIM-FC/NC was calculated for uncorrected and corrected data, using the mean of perfusion fraction values from runs 1 and 2. The corrected value was normalized to the uncorrected value and presented as a percentage. This analysis was performed on all volunteers in region A-L.

Volunteer	$f_{\text{Uncorrected}}$	$f_{\text{Temporal correction}}$ (%)	$f_{\text{Spatio-temporal correction}}$ (%)
A	2.199	4.680 (212.82)	3.205 (145.75)
B	3.691	3.025 (81.96)	2.458 (66.59)
C	3.243	2.852 (77.30)	2.875 (88.65)
D	3.216	2.486 (77.30)	1.711 (53.20)
E	3.202	3.172 (99.06)	3.026 (94.50)
F	3.788	1.351 (35.67)	2.395 (63.23)

The repeatability of the perfusion fraction was evaluated by calculating the ratio between the perfusion fractions obtained in two subsequent runs (run 1 and run 2) for all six volunteers. The results show that the two runs are not equally affected by signal drift, resulting in different perfusion fractions. On average for sIVIM, as shown in table 4.5, the perfusion fraction for both uncorrected and corrected data in run 1 is 8.8-9.93% higher than run 2. In a similar manner, the perfusion fraction in run 1 for IVIM-10b (as shown in table 4.6) is found to be between 14.8-17.9% higher than that in run 2. The same trend follows for IVIM-FC/NC, as shown in table 4.7, the perfusion fraction from run 1 is found to be 0.57-11.40% higher than run 2.

Table 4.5: The mean value of the absolute perfusion fraction ratio ($R = \frac{f_{run1}}{f_{run2}}$) and the mean difference ($1-\bar{R}$) from sIVIM, for the uncorrected and corrected data respectively. This analysis was performed on all volunteers in region A-L.

Volunteer	$R_{\text{Uncorrected}}$ (%)	$R_{\text{Temporal correction}}$ (%)	$R_{\text{Spatio-temporal correction}}$ (%)
A	113.00	110.90	112.20
B	114.50	114.70	114.10
C	111.10	109.70	111.20
D	107.50	106.30	107.10
E	99.00	97.90	99.60
F	114.50	113.80	114.10
Mean difference	-9.93	-8.88	-9.72

Table 4.6: The mean value of the absolute perfusion fraction ratio ($R = \frac{f_{run1}}{f_{run2}}$) and mean difference ($1 - \bar{R}$) from IVIM-10b, for the uncorrected and corrected data respectively. This analysis was performed on all volunteers in region A-L.

Volunteer	$R_{\text{Uncorrected}}$ (%)	$R_{\text{Temporal correction}}$ (%)	$R_{\text{Spatio-temporal correction}}$ (%)
A	104.10	109.70	108.60
B	85.20	88.30	78.70
C	100.10	102.10	101.30
D	94.50	98.70	98.40
E	108.00	112.10	112.40
F	117.90	117.30	114.10
Mean difference	- 17.90	-17.30	-14.80

Table 4.7: The mean value of the absolute perfusion fraction ratio ($R = \frac{f_{run1}}{f_{run2}}$) and the mean difference ($1 - \bar{R}$) from IVIM-FC/NC, for the uncorrected and corrected data respectively. This analysis was performed on all volunteers in region A-L.

Volunteer	$R_{\text{Uncorrected}}$ (%)	$R_{\text{Temporal correction}}$ (%)	$R_{\text{Spatio-temporal correction}}$ (%)
A	80.10	146.10	102.90
B	94.20	75.60	41.90
C	103.80	116.50	132.40
D	132.80	106.20	160.30
E	79.00	168.90	116.40
F	106.70	55.10	91.00
Mean difference	-0.57	-11.40	-7.48

5
Discussion

5.1 Preprocessing

Diffusion MRI (dMRI) is a complex and sensitive imaging technique, and various factors can affect the accuracy of the results. Preprocessing helps correct confounding factors and improve the data quality, making it easier to analyze and interpret. Some common preprocessing steps in dMRI include motion and distortion correction, denoising, and eddy current correction. These steps help to improve the signal-to-noise ratio and reduce artifacts in the data, which can improve the accuracy and reliability of the results.

Mapping out the appropriate preprocessing steps for intravoxel incoherent motion (IVIM) analysis can be difficult due to the lack of consensus on the optimal preprocessing pipeline for dMRI. The literature review of existing preprocessing tools for dMRI data revealed that some of these tools are designed for protocols with high b-values. FSL includes tools for the correction of motion artifacts, eddy current-induced distortions, outlier detection, susceptibility distortion, B_1 bias field, spatial normalization and brain extraction. While all of these tools can be useful in dMRI data preprocessing, only the brain extraction tool (BET), susceptibility correction, B_1 bias field correction and spatial normalization tools are directly applicable for IVIM. There are other tools that could be suited for IVIM, such as denosing methods, however, they require evaluation.

Some of the steps in the preprocessing pipeline for dMRI, such as, noise distribution bias, B_1 bias field correction and B-Matrix incompatibility might not be relevant for IVIM imaging. Generally, B-matrix incompatibility is not an issue for IVIM. However, in the studies of signal drift, it was found that this preprocessing step can be useful in situations where incompatibility does occur. The reason for this is that the chronological order of the b0-images is necessary for studying the signal drift over time. If the b-values and diffusion gradients direction are rearranged in a different order than the one specified, they lose their chronological order and can no longer be used for this purpose.

Preprocessing is a crucial step in IVIM analysis that can greatly impact the quality of the resulting parameter estimations. The specific preprocessing steps needed may vary depending on the data and the circumstances. In general, however, some key preprocessing correction steps that are often essential for obtaining good parameter estimations for IVIM include denoising, motion, susceptibility, Gibbs ringing, eddy current, Nyquist ghost and signal drift correction. The presence of these disturbances can make it difficult to accurately estimate IVIM parameters, as the oscillations in the signal can interfere with

the measurements. This can lead to underestimation or overestimation of parameters, such as the perfusion fraction. Appropriate correction methods to reduce or eliminate these artifacts are recommended.

5.2 Signal drift correction

Temporal signal drift was observed for all studied protocols: sIVIM, IVIM-10b, IVIM-FC and IVIM-NC. A signal decrease over time was the most common trend seen in the data that were acquired for all subjects. However, an increasing signal trend was also observed but with smaller magnitude. The repeated scans did not show the same trend in signal drift and varied in magnitude.

The maximum magnitude of signal drift for all volunteers except one was observed for the IVIM-10b protocol. The pulse sequence for sIVIM and IVIM-10b is the same, the only difference is the number of b-values used. IVIM-10b utilized 10 b-values as opposed to the three in sIVIM. The results could imply that the use of more b-values result in increased signal drift. The sequence for IVIM-FC/IVIM-NC differs from that of sIVIM/IVIM-10b, making comparison more difficult. It is possible that the differences observed between sIVIM and IVIM-10b may be attributed to the order in which the scans were performed, with sIVIM being scanned prior to IVIM-10b. It is worth noting, however, that this hypothesis has not been tested and it is unclear whether the opposite would have been observed if the order were reversed.

The temporal correction improved signal stabilization and reduced signal drift for the majority of scans. In one subject, two cases with a wider dispersion of signal drift were observed, which resulted in an insufficient temporal correction with similar dispersion as the uncorrected data. The reason for this dispersion in signal was not investigated further and is unclear, although, motion or heating have been suggested as potential contributing factors.

As shown in Chapter 4.3.2, the signal in white matter was found to vary both temporally and spatially. This suggests the need for correction for both effects. In general, the maximum signal drift was observed for IVIM-10b, while the least signal drift was observed for sIVIM.

The spatio-temporal correction analysis revealed that there was no spatial bias of the correction method and the signal drift effect between the regions of white matter that were studied. However, it was found that the signal drift did exhibit spatial variability. While the temporal correction did not amplify the signal drift to the same extent as the spatio-temporal correction, it is not necessarily a superior correction method because it does not address the spatial variations of the signal drift. It is worth noting that the effectiveness of a correction method should be evaluated in the context of the specific data and research goals being considered. However, there were cases in which the temporal correction outperformed the spatio-temporal correction without taking spatial variations

into account. On the other hand, there were also cases where the spatio-temporal correction performed better.

It is important to acknowledge that the analysis in this study did not correct for noise or other sources of interference. There are also other potential sources of error, such as the manually drawn areas of white matter analyzed, which may not have been homogeneous and could have introduced bias into the analysis. Additionally, these masks were created from the first volume of each protocol. Manual observation was used to adjust the areas to fit last and first volume within a series of protocols, without considering the intermediate volumes. Furthermore, since Dynamic Stabilization was not performed for the acquired volumes, the potential benefits of updating the center of frequency were not explored in this study. It is possible that Dynamic Stabilization could have improved the results, but this was not investigated.

The perfusion fraction is a measure that can provide insight into the microcirculatory functioning of a tissue or organ. It is related to the proportion of blood flow and oxygenation within a given region. It is important to note that the accuracy of the perfusion fraction can be affected by factors such as signal drift, which can cause the estimated perfusion fraction to be too high or too low. As there was no reference for the true perfusion fraction, it is difficult to determine which correction approach was superior. The perfusion fractions obtained during the different runs (run 1 and run 2) are not identical. On average, for all scans, the perfusion fraction obtained during run 1 was found to be higher than in run 2. This may suggest that the true perfusion fraction may be closer to the mean value of multiple consecutive runs.

While it is difficult to determine the relative effectiveness of different correction methods without a reference standard, the results of this study did show a bigger difference between the corrected and uncorrected perfusion fraction for the IVIM-FC/NC protocol compared to the sIVIM and IVIM-10b. These differences suggest that the effectiveness of correction methods may vary depending on the protocol used, and further research is needed to understand the underlying factors that contribute to these variations.

5.3 Future perspectives

Several factors can impact the magnitude of the observed signal drift and its effect on IVIM parameter estimates, including the protocol and signal model used for parameter estimation. Our results indicate that even with the use of temporal and spatio-temporal corrections, residual signal drift may still be present. While complete elimination of signal drift may not be feasible, it is important to minimize it as much as possible in order to enhance the reliability of the data. To this end, we recommend that correction methods be optimized for a given protocol. It would be ideal to propose a general signal drift correction method. However, in order to accomplish this, it is necessary to establish a standardized protocol for IVIM imaging. At present, there is no widely accepted standardized protocol for IVIM imaging or preprocessing pipeline.

Both correction methods make assumptions about the pattern of signal drift. Hansen et al. proposed that the effects of signal drift vary spatially and over time, while Vos et al. proposed a global temporal correction that does not take spatial variability into account [4, 11]. These two strategies have been found to both decrease or increase the magnitude of signal drift in IVIM data. It is however, important to investigate the characteristics of signal drift and its causes in order to identify the most appropriate approach.

6
Conclusions

There is currently no consensus on the optimal preprocessing approach for intravoxel incoherent motion (IVIM) analysis. Many tools for diffusion-weighted magnetic resonance imaging (dMRI) cannot be used directly on IVIM datasets and require modification. Standardizing both protocols and preprocessing tools would improve reproducibility and increase the reliability of research in this field.

While the temporal correction and the spatio-temporal correction can help to reduce the effects of the observed signal drift in IVIM-data, they are not able to completely eliminate it. There are cases where the corrected data may enhance signal drift effects more than the uncorrected data. Therefore, it may be necessary to use additional methods to fully correct for signal drift in order to obtain reliable results from IVIM imaging.

Bibliography

[1] Denis Le Bihan. What can we see with ivim mri? *NeuroImage*, 187:56–67, 2019. Physiological and Quantitative MRI. URL: https://www.sciencedirect.com/science/article/pii/S1053811917310868, doi:https://doi.org/10.1016/j.neuroimage.2017.12.062.

[2] Denis Le Bihan, Eric Breton, Denis Lallemand, Marie-Louise Aubin, Jacqueline Vignaud, and Maurice Laval-Jeantet. Separation of Diffusion and Perfusion in Intravoxel Incoherent Motion MR Imaging. *Radiology*, 168:497–505, 8 1988. doi:10.1148/radiology.168.2.3393671.

[3] Christian Federau Eric E. Sigmund Denis Le Bihan, Mami Iima. *Intravoxel Incoherent Motion (IVIM) MRI : Principles and Applications*. Jenny Stanford Publishing, 1 edition, 2018.

[4] Sjoerd B. Vos, Chantal M. W. Tax, Peter R. Luijten, Sebastien Ourselin, Alexander Leemans, and Martijn Froeling. The importance of correcting for signal drift in diffusion mri. *Magnetic Resonance in Medicine*, 77(1):285–299, 2017. URL: https://onlinelibrary.wiley.com/doi/abs/10.1002/mrm.26124, arXiv:https://onlinelibrary.wiley.com/doi/pdf/10.1002/mrm.26124, doi:https://doi.org/10.1002/mrm.26124.

[5] Chantal M.W. Tax, Matteo Bastiani, Jelle Veraart, Eleftherios Garyfallidis, and M. Okan Irfanoglu. What's new and what's next in diffusion mri preprocessing. *NeuroImage*, 249:118830, 2022. URL: https://www.sciencedirect.com/science/article/pii/S1053811921011010, doi:https://doi.org/10.1016/j.neuroimage.2021.118830.

[6] Donald W. McRobbie, Elizabeth A. Moore, Martin J. Graves, and Martin R. Prince. *MRI From Picture to Proton*. Cambridge University Press, 2 edition, 2006.

[7] Denis Le Bihan and Robert Turner. The capillary network: a link between ivim and classical perfusion. *Magnetic Resonance in Medicine*, 27(1):171–178, 1992. URL: https://onlinelibrary-wiley-com.ezproxy.ub.gu.se/doi/abs/10.1002/mrm.1910270116, arXiv:https://onlinelibrary-wiley-com.ezproxy.ub.gu.se/doi/pdf/10.1002/mrm.1910270116, doi:https://doi-org.ezproxy.ub.gu.se/10.1002/mrm.1910270116.

[8] Stephen M. Smith. Fast robust automated brain extraction. *Human Brain Mapping*, 17(3):143–155, 2002. URL: https://onlinelibrary.wiley.com/doi/abs/10.1002/hbm.10062, arXiv:https://onlinelibrary.wiley.com/doi/pdf/10.1002/hbm.10062, doi:https://doi.org/10.1002/hbm.10062.

[9] Ben Jeurissen, Alexander Leemans, and Jan Sijbers. Automated correction of improperly rotated diffusion gradient orientations in diffusion weighted mri. *Medi-*

cal Image Analysis, 18(7):953–962, 2014. URL: https://www.sciencedirect.com/science/article/pii/S1361841514000930, doi:https://doi.org/10.1016/j.media.2014.05.012.

[10] Robert W. Cox. Afni: Software for analysis and visualization of functional magnetic resonance neuroimages. *Computers and Biomedical Research*, 29(3):162–173, 1996. URL: https://www.sciencedirect.com/science/article/pii/S0010480996900142, doi:https://doi.org/10.1006/cbmr.1996.0014.

[11] Colin B. Hansen, Vishwesh Natha, Allison E Hainline, Kurt G. Schilling, Prasanna Parvathaneni, Roza G. Bayrak, Justin A. Blaber, Okan Irfanoglu, Carlo Pierpaoli, Adam W. Anderson, Baxter P. Rogers, and Bennett A. Landman. Characterization and correlation of signal drift in diffusion weighted mri. *Magnetic Resonance Imaging,*, 57(April):133–142, 2019.

[12] Elias Kellner, Bibek Dhital, Valerij G. Kiselev, and Marco Reisert. Gibbs-ringing artifact removal based on local subvoxel-shifts. *Magnetic Resonance in Medicine*, 76(5):1574–1581, 2016. URL: https://onlinelibrary.wiley.com/doi/abs/10.1002/mrm.26054, arXiv:https://onlinelibrary.wiley.com/doi/pdf/10.1002/mrm.26054, doi:https://doi.org/10.1002/mrm.26054.

[13] Santiago Aja-Fernández, Véronique Brion, and Antonio Tristán-Vega. Effective noise estimation and filtering from correlated multiple-coil mr data. *Magnetic Resonance Imaging*, 31(2):272–285, 2013. URL: https://www.sciencedirect.com/science/article/pii/S0730725X12002822, doi:https://doi.org/10.1016/j.mri.2012.07.006.

[14] Shreyas Fadnavis, Joshua Batson, and Eleftherios Garyfallidis. Patch2self: Denoising diffusion MRI with self-supervised learning. *CoRR*, abs/2011.01355, 2020. URL: https://arxiv.org/abs/2011.01355, arXiv:2011.01355.

[15] Jesper L.R. Andersson and Stamatios N. Sotiropoulos. An integrated approach to correction for off-resonance effects and subject movement in diffusion mr imaging. *NeuroImage*, 125:1063–1078, 2016. URL: https://www.sciencedirect.com/science/article/pii/S1053811915009209, doi:https://doi.org/10.1016/j.neuroimage.2015.10.019.

[16] Julian Maclaren, Michael Herbst, Oliver Speck, and Maxim Zaitsev. Prospective motion correction in brain imaging: A review. *Magnetic Resonance in Medicine*, 69(3):621–636, 2013. URL: https://onlinelibrary.wiley.com/doi/abs/10.1002/mrm.24314, arXiv:https://onlinelibrary.wiley.com/doi/pdf/10.1002/mrm.24314, doi:https://doi.org/10.1002/mrm.24314.

[17] Jesper L.R. Andersson, Stefan Skare, and John Ashburner. How to correct susceptibility distortions in spin-echo echo-planar images: application to diffusion tensor imaging. *NeuroImage*, 20(2):870–888, 2003. URL: https://www.sciencedirect.com/science/article/pii/S1053811903003367, doi:https://doi.org/10.1016/S1053-8119(03)00336-7.

[18] Qing X. Yang, Stefan Posse, Denis Le Bihan, and Michael B. Smith. Double-sampled echo-planar imaging at 3 tesla. *Journal of Magnetic Resonance, Series B*, 113(2):145–150, 1996. URL: https://www.sciencedirect.com/science/article/pii/S1064186696901673, doi:https://doi.org/10.1006/jmrb.1996.0167.

[19] Colin B. Hansen, Baxter P. Rogers, Kurt G. Schilling, Vishwesh Nath, Justin A. Blaber, Okan Irfanoglu, Alan Barnett, Carlo Pierpaoli, Adam W. Anderson,

and Bennett A. Landman. Empirical field mapping for gradient nonlinearity correction of multi-site diffusion weighted mri. *Magnetic Resonance Imaging*, 76:69–78, 2021. URL: https://www.sciencedirect.com/science/article/pii/S0730725X20306408, doi:https://doi.org/10.1016/j.mri.2020.11.005.

[20] Yoojin Lee, Adam O. Kettinger, Bertram Jakob Wilm, Ralf Deichmann, Nikolaus Weiskopf, Christian Lambert, Klaas Paul Pruessmann, and Zoltan Nagy. A comprehensive approach for correcting voxel-wise b-value errors in diffusion mri. *Magnetic Resonance in Medicine*, 83(6):2173–2184, 2020. URL: https://onlinelibrary.wiley.com/doi/abs/10.1002/mrm.28078, arXiv:https://onlinelibrary.wiley.com/doi/pdf/10.1002/mrm.28078, doi:https://doi.org/10.1002/mrm.28078.

[21] Steen Moeller, Pramod Pisharady Kumar, Jesper Andersson, Mehmet Akcakaya, Noam Harel, Ruoyun(Emily) Ma, Xiaoping Wu, Essa Yacoub, Christophe Lenglet, and Kamil Ugurbil. Diffusion imaging in the post hcp era. *Journal of Magnetic Resonance Imaging*, 54(1):36–57, 2021. URL: https://onlinelibrary.wiley.com/doi/abs/10.1002/jmri.27247, arXiv:https://onlinelibrary.wiley.com/doi/pdf/10.1002/jmri.27247, doi:https://doi.org/10.1002/jmri.27247.

[22] Y. Zhang, M. Brady, and S. Smith. Segmentation of brain mr images through a hidden markov random field model and the expectation-maximization algorithm. *IEEE Transactions on Medical Imaging*, 20(1):45–57, 2001. doi:10.1109/42.906424.

[23] Stephen M. Smith, Mark Jenkinson, Heidi Johansen-Berg, Daniel Rueckert, Thomas E. Nichols, Clare E. Mackay, Kate E. Watkins, Olga Ciccarelli, M. Zaheer Cader, Paul M. Matthews, and Timothy E.J. Behrens. Tract-based spatial statistics: Voxelwise analysis of multi-subject diffusion data. *NeuroImage*, 31(4):1487–1505, 2006. URL: https://www.sciencedirect.com/science/article/pii/S1053811906001388, doi:https://doi.org/10.1016/j.neuroimage.2006.02.024.

[24] Hui Zhang, Paul A. Yushkevich, Daniel C. Alexander, and James C. Gee. Deformable registration of diffusion tensor mr images with explicit orientation optimization. *Medical Image Analysis*, 10(5):764–785, 2006. The Eighth International Conference on Medical Imaging and Computer Assisted Intervention – MICCAI 2005. URL: https://www.sciencedirect.com/science/article/pii/S1361841506000417, doi:https://doi.org/10.1016/j.media.2006.06.004.

[25] M. Okan Irfanoglu, Amritha Nayak, Jeffrey Jenkins, Elizabeth B. Hutchinson, Neda Sadeghi, Cibu P. Thomas, and Carlo Pierpaoli. Dr-tamas: Diffeomorphic registration for tensor accurate alignment of anatomical structures. *NeuroImage*, 132:439–454, 2016. URL: https://www.sciencedirect.com/science/article/pii/S1053811916001750, doi:https://doi.org/10.1016/j.neuroimage.2016.02.066.

[26] Paul A. Yushkevich, Joseph Piven, Heather Cody Hazlett, Rachel Gimpel Smith, Sean Ho, James C. Gee, and Guido Gerig. User-guided 3D active contour segmentation of anatomical structures: Significantly improved efficiency and reliability. *Neuroimage*, 31(3):1116–1128, 2006. URL: www.itksnap.org.

A

Appendix 1

A.1 Expansion of Hansen et al. spatio-temporal correction

Hansen et al. expanded the temporal correction to address the spatial variations of signal drift [11]. The estimation of the signal drift for each voxel is given by following formula,

$$V(X,n) = B_T(X,n) + B_{TSv}(X,n) + B_{TSn}(X,n) + B_{TSn^2}(X,n) + v_{0,x} \tag{A.1}$$

where X is a vector containing the x,y,z coordinates for the given voxel and n is the image. $B_T(X,n), B_{TSv}(X,n), B_{TSn}(X,n)$ and $B_{TSn^2}(X,n)$ are polynomials and given by:

$$B_T(X,n) = d_1n^2 + d_2n \tag{A.2}$$

$$\begin{aligned} B_{TSv}(X,n) = v_{0,X}(&d_3x + d_4y + d_5z + d_6xy + d_7xz + d_8yz + d_9xyz \\ &+d_{10}x^2 + d_{11}y^2 + d_{12}z^2 + d_{13}xy^2 + d_{14}xz^2 + d_{15}xy^2z + d_{16}xyz^2 \\ &+d_{17}xy^2z^2 + d_{18}x^2y + d_{19}x^2z + d_{20}x^2yz + d_{21}x^2y^2 + d_{22}x^2z^2 \\ &+d_{23}x^2y^2z + d_{24}x^2y^{z^2} + d_{25}x^2y^2z^2 + d_{26}y^2z + d_{27}yz^2 + d_{28}y^2z^2) \end{aligned} \tag{A.3}$$

$$\begin{aligned} B_{TSn}(X,n) = n(&d_{29}x + d_{30}y + d_{31}z + d_{32}xy + d_{33}xy + d_{34}yz \\ &+d_{35}xyz + d_{36}x^2 + d_{37}y^2 + d_{38}z^2 + d_{39}xy^2 + d_{40}xz^2 \\ &+d_{41}xy^2z + d_{42}xyz^2 + d_{43}xy^2z^2 + d_{44}x^2y + d_{45}x^2z + d_{46}x^2yz \\ &+d_{47}x^2y^2 + d_{48}x^2z^2 + d_{49}x^2y^2z + d_{50}x^2yz^2 + d_{51}x^2y^2z^2 \\ &+d_{52}y^2z + d_{53}yz^2 + d_{54}y^2z^2) \end{aligned} \tag{A.4}$$

$$\begin{aligned} B_{TSn^2} = n^2(&d_{55}x + d_{56}y + d_{57}z + d_{58}xy + d_{59}xz + d_{60}yz \\ &+d_{61}xyz + d_{62}x^2 + d_{63}y^2 + d_{64}z^2d_{65}xy^2 + d_{66}xz^2 \\ &+d_{67}xy^2z + d_{68}xyz^2 + d_{69}xy^2z^2 + d_{70}x^2y + d_{71}x^2z + d_{72}x^2yz \\ &+d_{73}x^2y^2 + d_{74}x^2z^2 + d_{75}x^2y^2z + d_{76}x^2yz^2 + d_{77}x^2y^2z^2 \\ &+d_{78}y^2z + d_{79}yz^2 + d_{80}y^2z^2) \end{aligned} \tag{A.5}$$

The function $B_T(X,n)$ accounts for temporal effects.$B_{TSv}(X,n)$, $B_{TSn}(X,n)$, and $B^2_{TSn}(X,n)$ are Chebyshev polynomials that represent the spatial-temporal components in the model.

A.2 Temporal correction

This section contains the results of uncorrected and temporally corrected signal, for the six healthy volunteers studied. The volunteers are refereed to as A, B, C, D, E and F.

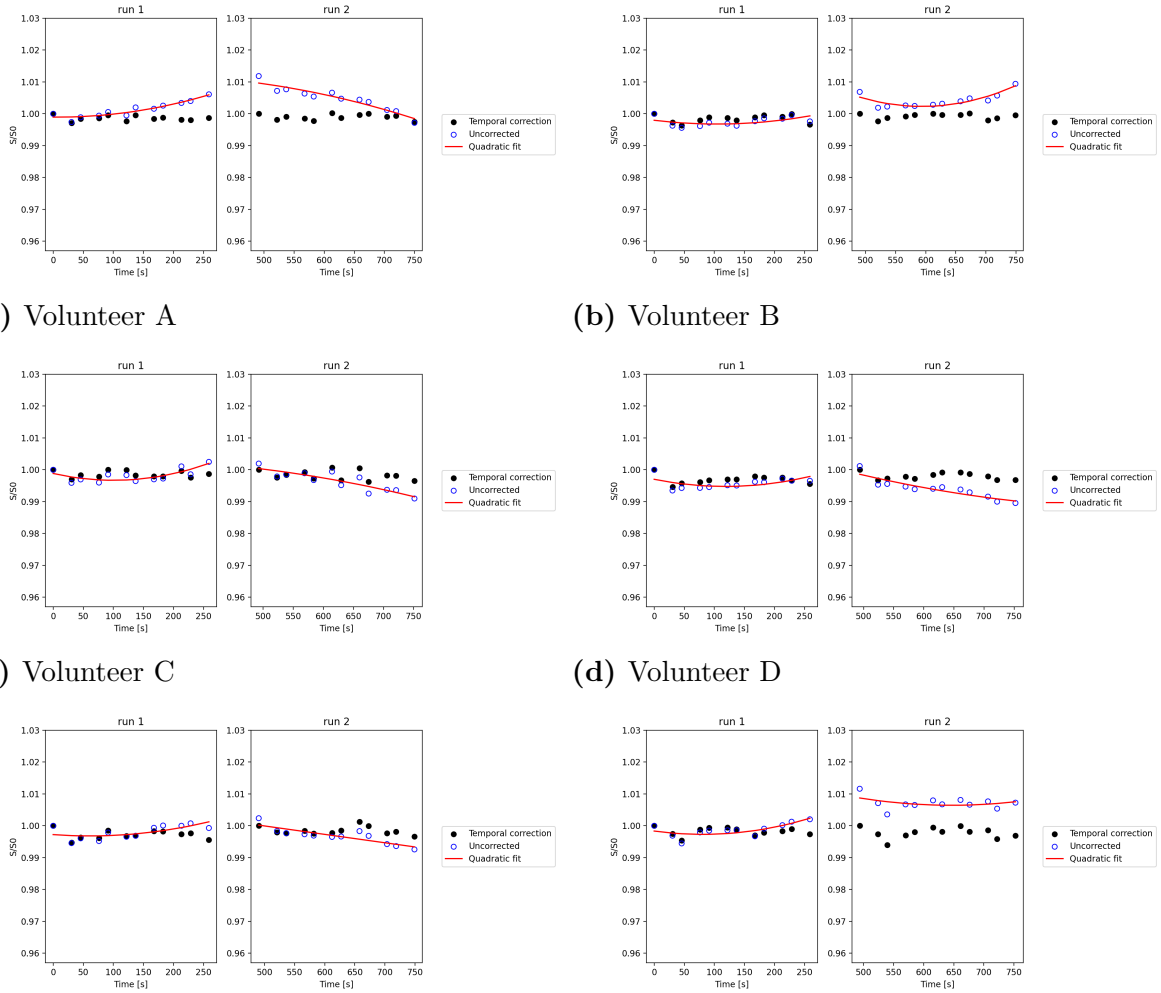

(a) Volunteer A

(b) Volunteer B

(c) Volunteer C

(d) Volunteer D

(e) Volunteer E

(f) Volunteer F

Figure A.1: Uncorrected and temporally corrected data from six healthy volunteers, from sIVIM.

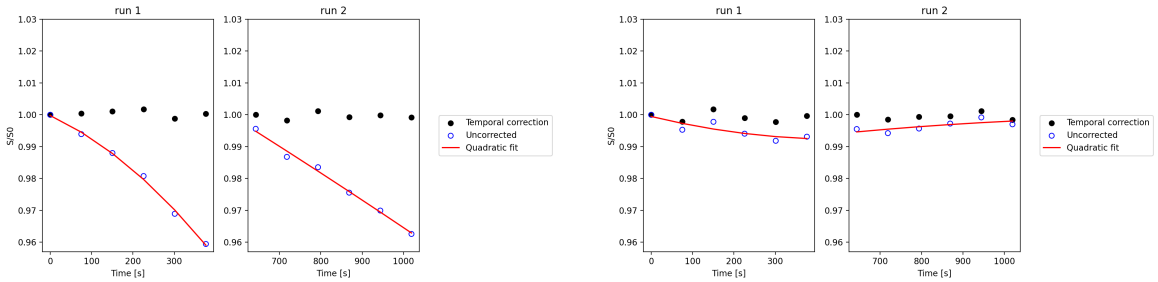

(a) Volunteer A

(b) Volunteer B

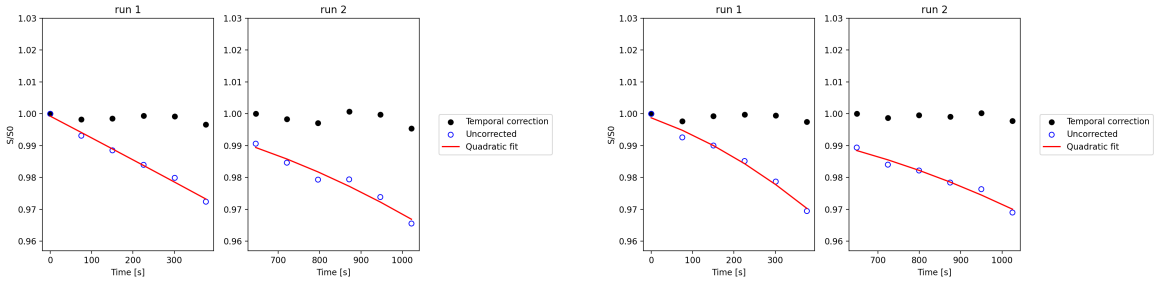

(c) Volunteer C

(d) Volunteer D

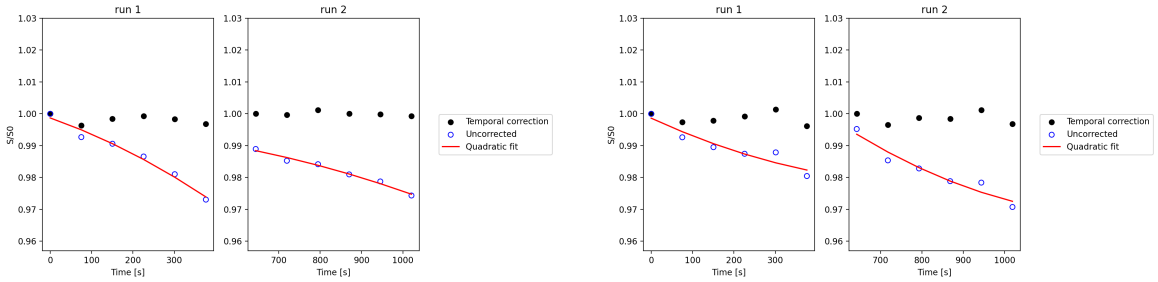

(e) Volunteer E

(f) Volunteer F

Figure A.2: Uncorrected and temporally corrected data from six healthy volunteers, from IVIM-10b.

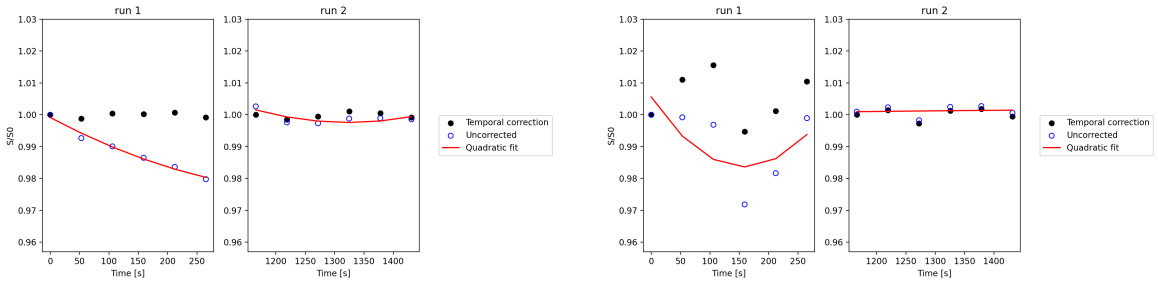

(a) Volunteer A

(b) Volunteer B

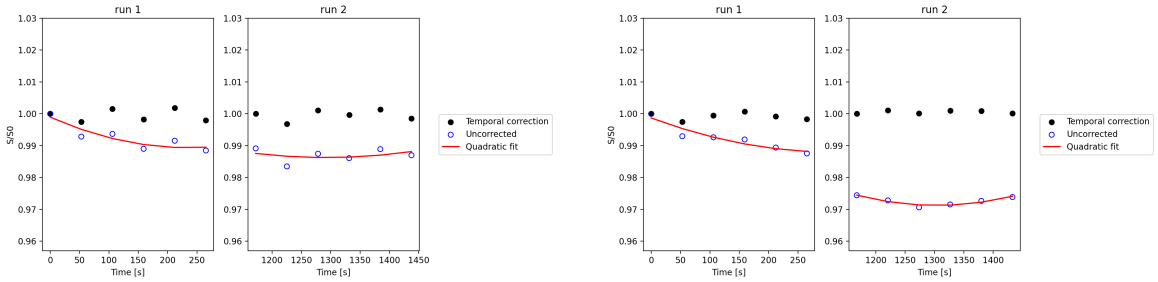

(c) Volunteer C

(d) Volunteer D

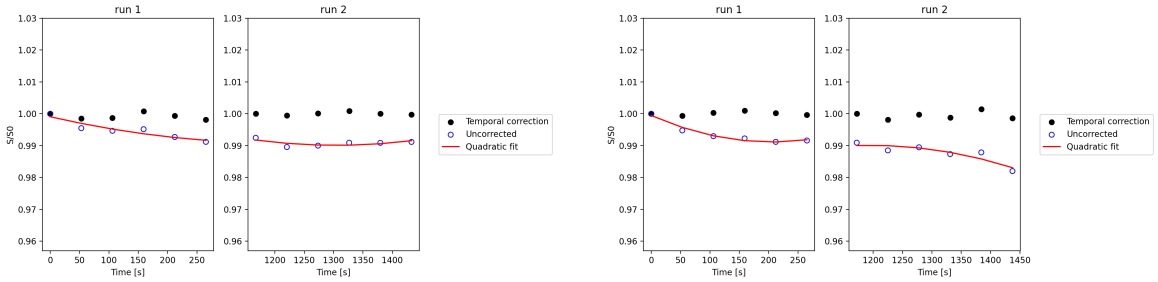

(e) Volunteer E

(f) Volunteer F

Figure A.3: Uncorrected and temporally corrected data from six healthy volunteers, from IVIM-FC.

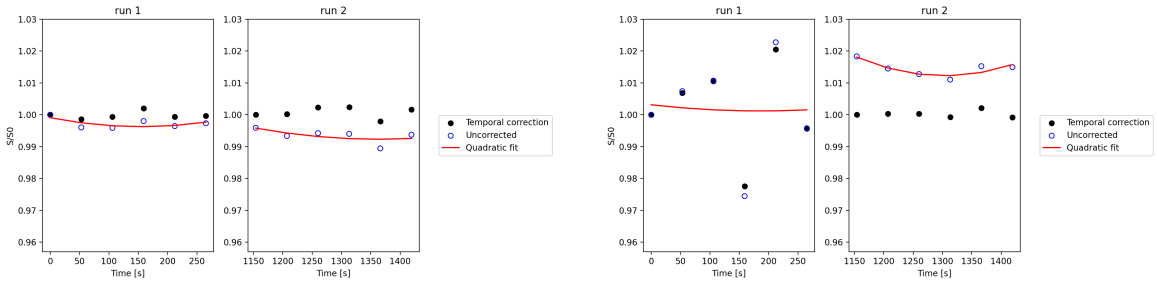

(a) Volunteer A

(b) Volunteer B

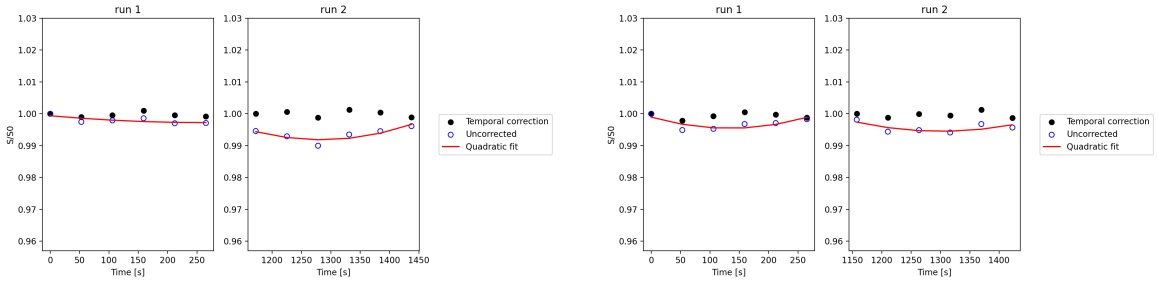

(c) Volunteer C

(d) Volunteer D

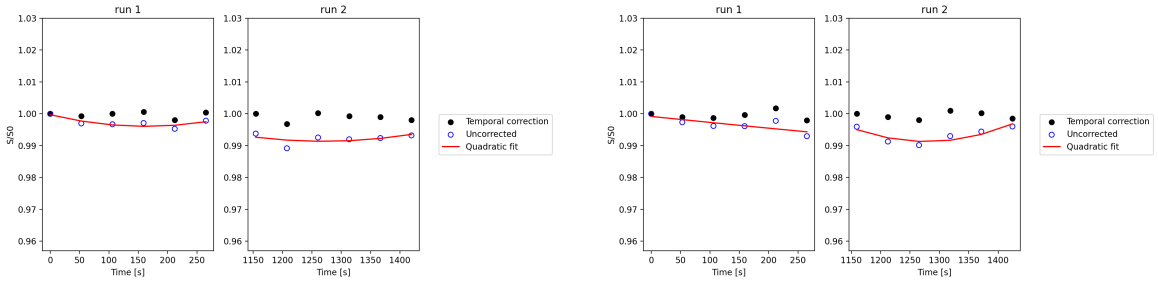

(e) Volunteer E

(f) Volunteer F

Figure A.4: Uncorrected and temporally corrected data from six healthy volunteers, from IVIM-NC.